Desmosomal COP9 regulates proteome degradation in arrhythmogenic right ventricular dysplasia/cardiomyopathy

Yan Liang[1], Robert C. Lyon[1], Jason Pellman[1], William H. Bradford[1], Stephan Lange[1,2], Julius Bogomolovas[1], Nancy D. Dalton[1], Yusu Gu[1], Marcus Bobar[1], Mong-Hong Lee[3], Tomoo Iwakuma[4], Vishal Nigam[5,6], Angeliki Asimaki[7], Melvin Scheinman[8], Kirk L. Peterson[1] and Farah Sheikh[1*]

[1]Department of Medicine, University of California San Diego, 9500 Gilman Drive, La Jolla, CA, 92093, USA; [2]Institute of Medicine, Department of Molecular and Clinical Medicine and Wallenberg Centre for Molecular and Translational Medicine, University of Gothenburg, Gothenburg, Sweden; [3]Department of Molecular and Cellular Oncology, The University of Texas MD Anderson Cancer Center, Houston, TX, 77030, USA; [4]Department of Cancer Biology, University of Kansas Medical Center, Kansas City, KS, 66010, USA; [5]Department of Pediatrics, University of California San Diego, 9500 Gilman Drive, La Jolla, CA, 92093, USA; [6]Department of Pediatrics, Seattle Children's Research Institute and University of Washington, 1900 Ninth Ave, Seattle, WA, 98101, USA; [7]Cardiology Clinical Academic Group, St. George's University of London, Cranmer Terrace, London, UK; [8]Department of Medicine, Cardiac Electrophysiology Section, University of California San Francisco, 500 Parnassus Avenue, San Francisco, CA, 94143, USA

Corresponding author: Farah Sheikh, Department of Medicine, University of California San Diego, 9500 Gilman Drive, La Jolla, CA, 92093-0613C. Tel: (858) 246-0754, Fax: (858) 822-1355; email address: fasheikh@health.ucsd.edu

Conflict of interest statement

F.S. is a co-founder of Stelios Therapeutics Inc. (previously known as ARVC Therapeutics Inc.)

Abstract

Dysregulated protein degradative pathways are increasingly recognized as mediators of human disease. This mechanism may have particular relevance to desmosomal proteins that play critical structural roles in both tissue architecture and cell-cell communication as destabilization/breakdown of the desmosomal proteome is a hallmark of genetic-based desmosomal-targeted diseases, such as the cardiac disease, arrhythmogenic right ventricular dysplasia/cardiomyopathy (ARVD/C). However, no information exists on whether there are resident proteins that regulate desmosomal proteome homeostasis. Here we uncovered a cardiac COP9 desmosomal resident protein complex, composed of subunit 6 of the COP9 signalosome (CSN6), that enzymatically restricted neddylation and targeted desmosomal proteome degradation. CSN6 binding, localization, levels and function were impacted in hearts of classic mouse and human models of ARVD/C impacted by desmosomal loss and mutations, respectively. Loss of desmosomal proteome degradation control due to junctional reduction/loss of CSN6 and human desmosomal mutations destabilizing junctional CSN6 were also sufficient to trigger ARVD/C in mice. We identified a desmosomal resident regulatory complex that restricted desmosomal proteome degradation and disease.

Introduction

The heart requires precise spatiotemporal control of cardiac protein turnover at distinct subcellular locations to maintain cardiac function as dysregulated protein degradative pathways are increasingly recognized as mediators of human cardiac disease (1-3). These pathways may have special relevance to desmosomal proteins, which play critical structural roles in both tissue architecture and cell-cell communication, especially in organs that undergo constant mechanical stress, such as the heart (4, 5).

Five classic proteins encompass the cardiac desmosomal cell-cell junction protein complex, which we loosely term, "desmosomal proteome", act to resist mechanical insult, which include desmoplakin (DSP), a central linker that tethers the tissue-specific desmosomal cadherins (desmoglein-2 (DSG2) and desmocollin-2 (DSC2)), to the intracellular intermediate filament cytoskeleton (desmin), through the intermediary armadillo proteins (plakoglobin (PKG) and plakophilin-2 (PKP2)) (4, 5). In the heart, the desmosomal complex acts alongside another mechanical junction, termed the fascia adherens junction (associated with actin cytoskeleton) as well as electrical channels, known as gap junctions to altogether synchronize muscle contraction (6). Genetic mutations in desmosomal genes, resulting in the destabilization/breakdown of the desmosomal proteome is a central hallmark of all genetic-based desmosomal-targeted diseases (4, 7), including the cardiac disease, arrhythmogenic right ventricular dysplasia/cardiomyopathy (ARVD/C) (8, 9). Protein degradation is a critical part of protein quality control and mainly performed by two pathways which include the ubiquitin-proteasome system and autophagy-lysosome pathway (3). These pathways recycle damaged, misfolded, or unneeded proteins into free amino acids for future use (3). The cardiac cell-cell junction is thought to display signs of active protein degradation as ubiquitin conjugates, autophagosomes and markers of ubiquitin-

mediated selective autophagy have been localized to these locations in both healthy and diseased cardiomyocytes (10-14). However, no information exists on whether there are resident proteins that regulate desmosomal (cell junction) proteome homeostasis.

Using an unbiased yeast-two-hybrid screen to search for desmosomal proteome regulators in the adult human heart, in combination with *in silico* molecular docking, *in vivo* genetic mouse and human heart tissue studies, we reveal protein degradation machinery that uniquely target the cardiac desmosome to regulate desmosomal proteome longevity and function. We identify constitutive photo-morphogenesis 9 signalosome subunit 6 (CSN6), a member of a pathway classically associated with protein quality control, as a resident desmosomal protein that endogenously restricts desmosome protein degradation to prevent the cardiac desmosomal targeted disease, ARVD/C, in mouse and man.

Results

Identification of COP9 signalosome subunit 6 as a resident cardiac desmosomal protein. To identify proteins regulating cardiac desmosomal proteome homeostasis, we performed an unbiased yeast-two-hybrid screen using the human DSP N-terminus (1-519 amino acids) as bait and an adult human heart cDNA library as prey. DSP was selected as it is a central component in the desmosomal complex and the N-terminus was selected, as it is a major hub for interactions with desmosomal (armadillo) proteins (4) and "hotspot" for pathogenic ARVD/C mutations (15). We identified full-length constitutive photo-morphogenesis 9 signalosome subunit 6 (CSN6) as an interacting partner of DSP N-terminus in the adult human heart. Forced yeast-two-hybrid assays validated the interaction between DSP N-terminus and CSN6 (Figure 1A). *In silico* studies taking advantage of existing DSP and CSN6 crystal structures (16, 17) also showed that DSP and CSN6 structurally interfaced as DSP N-terminus (amino acids 179-625) could structurally complex with the signature Mpr1, Pad1 N-terminal (MPN) domain of CSN6 (Figure 1B). In the adult mouse heart, endogenous CSN6 co-immunoprecipitated with endogenous DSP as well as the desmosomal armadillo protein, PKP2 (Figure 1C). *Csn6* knockout (*Csn6*-iKO) heart extracts and IgG serum controls were used to demonstrate the specificity of CSN6 interactions to DSP and PKP2 (Figure 1C). CSN6 is also expressed in insoluble (junctional-enriched) fractions and co-localized with DSP at the cardiac cell-cell junction in adult mouse hearts (Figure 1D and E). Cardiac-specific *Dsp* knockout hearts also displayed a striking reduction in CSN6 protein levels (insoluble fraction) and localization at the cardiac cell-cell junction (Figure 1D and E), highlighting CSN6 as an integral component of the cardiac desmosomal complex.

Cardiac CSN6 loss selectively accelerates desmosomal protein degradation in vivo. The COP9 signalosome (CSN), composed of eight subunits (CSN1-CSN8) is evolutionarily conserved in

eukaryotes and thought to have multi-faceted roles in controlling ubiquitin-mediated protein degradation as well as acting as a signaling docking hub (18-20). However, the biological role of CSN6 in the heart has remained unclear. To determine the role of CSN6 in the postnatal heart *in vivo*, we generated two cardiac-specific *Csn6* knockout mice (Supplemental Figure 1A-C) by using cardiac-specific a-myosin-heavy chain (MHC)-Cre and cardiac-inducible a-MHC-MerCreMer mouse lines to assess its role in the early postnatal and adult heart, respectively (21, 22). Protein analyses revealed that CSN6 protein levels and junctional localization were lost in *Csn6* knockout hearts (Supplemental Figure 1D-G). Given the direct protein interactions between CSN6 and DSP, we sought to assess the impact of CSN6 loss on the desmosomal proteome. CSN6 loss accelerated desmosomal protein complex destruction as *Csn6* knockout hearts displayed selective loss of desmosomal protein levels when compared to controls (Figure 2). At early ages, mice harboring cardiac CSN6 loss resulted in primary loss of DSP as well as the gap junction (electrical) protein, connexin43 in mice (Figure 2A and C), which we have previously shown to be an early target of DSP loss (23). These early defects culminated into the total and specific destruction/loss of the desmosomal proteome at late ages in mice (Figure 2B and D). We further highlight that global effects on the cardiomyocyte were not observed as proteins residing in non-desmosomal (eg., fascia adherens junction and costamere/plasma membrane proteins) structures within cardiomyocytes were not significantly impacted in *Csn6* knockout hearts (Figure 2B and D). RNA expression of desmosomal genes was also not impacted in *Csn6* knockout hearts (Supplemental Figure 2), highlighting a post-transcriptional role for CSN6 within the desmosomal protein complex.

CSN6 loss renders the cardiomyocyte susceptible to hyper-neddylation and targeted desmosomal protein degradation. Classic protein functions of CSNs are to enzymatically de-neddylate and

inactivate cullin RING E3 ubiquitin ligases (CURLs) to regulate ubiquitin-mediated protein degradation of targeted substrates (24). *In vitro* reconstitution assays refining the minimal CSN subunits required for de-neddylation activity defined that the CSN5-CSN6 heterodimer is sufficient and required to trigger de-neddylation activity (17, 25), thus, we also sought to assess CSN5 localization in the adult mouse heart in the absence and presence of CSN6. We reveal that CSN5 is also localized to the cardiac cell junction in adult mouse hearts, similar to CSN6 (Figure 3A). Furthermore, we show that its cell junction localization was dependent on the presence of CSN6 as cardiac loss of CSN6 resulted in loss of CSN5 cell-cell junction localization and levels (Figure 3A), highlighting the presence of an active CSN subcomplex (consisting of CSN5 and CSN6) at the cardiac desmosome.

We further showed that CSN6 loss directly impacted cullin neddylation mediated control as a select group of CURLs, namely cullin 1 and cullin 3 (migrate between 80-88 kDa) displayed a dramatic increase in their neddylated (higher molecular weight) forms in CSN6 knockout hearts (Figure 3B and E). Immunofluorescence microscopy studies further revealed that CURLs that are directly impacted (hyperneddylated) by CSN6 loss (eg., cullin 3) are also localized to cell-cell junctions (Supplemental Figure 3). Consistent with these findings we observed a striking increase in neddylation (at the 80-88 kDa range) as well as ubiquitination, a downstream target of neddylation in *Csn6* knockout hearts (Figure 3C, D, F and G). Cross-talk between ubiquitination and selective autophagy-mediated pathways was also evident as p62 levels were significantly upregulated in insoluble fractions of *Csn6* knockout hearts (Figure 3D and G). These observations are consistent with restricted effects of CSN6 loss at the cell-cell junction as ultrastructural observations of hyper-accumulation of autophagic machinery was only observed at the cardiac cell-cell junction alongside destruction/loss of desmosomal structures (Figure 3H). Specifically,

Csn6 knockout hearts revealed early defects in desmosomal integrity, which included the hyper-accumulation of autophagic vacuoles (red arrowheads) at remnants of destroyed electron dense desomosomes (eg., often observed as wider/half desmosomal structures (yellow arrowheads); Figure 3H). *Csn6* knockout hearts also displayed hyper-accumulation of autophagic-like (multi-layered) vesicles (green arrowhead) specifically at the cardiac cell junction (Figure 3H). The sufficiency of *Csn6* loss (Cre group) to target increased neddylation and ensuing ubiquitination was also observed in cardiomyocytes (Figure 4A and D and Supplemental Figure 4A). Using cycloheximide chase assays, we show that CSN6 deficiency in cardiomyocytes results in a significant reduction in the half-life of key/core desmosomal proteins (which undergo more rapid degradation), demonstrating that protein degradation is specifically impacted in *Csn6* deficient cardiomyocytes (Figure 4B and C). Restoration of CSN enzymatic function (via neddylation inhibitor MLN4924) and thus, targeting underlying deneddylation functions of CSN6 can also alleviate desmosomal protein loss caused by deletion of CSN6 (Figure 4D), highlighting desmosomal proteins as direct substrates of neddylation-mediated protein degradation.

Disruption of the CSN6-desmosomal complex and protein degradation pathways underlies ARVD/C in mice and man. To determine the broad relevance of CSN6 pathways in desmosomal targeted diseases, we sought to assess CSN6 binding, localization, levels and function in classic mouse and human models of ARVD/C impacted by classic desmosomal loss/mutations. Hyper-neddylation, hyper-ubiquitination and an increase in p62 levels was observed in hearts of cardiac-specific *Dsp* knockout mice (Figure 5A and Supplemental Figure 4B), which harbored classic ARVD/C features (23) and a reduction in CSN6 localization at the cardiac cell-cell junction (Figure 1D and E). Furthermore, ultrastructural analyses revealed hyper-accumulation of autophagic machinery at the cardiac cell-cell junction alongside destruction/loss of desmosomal

structures (Figure 5B), similar to *Csn6* knockout hearts (Figure 3H). To determine if CSN6 pathways are disrupted in human ARVD/C, we identified a patient with a clinical diagnosis of ARVD/C that carried a previously identified desmoplakin (*DSP*) *R315C* missense mutation (26) and pathogenic *PKP2 IVS10-1 G>C* splice site mutation (27, 28). This patient provided a genetic platform to assess the importance of the CSN6-desmosomal interaction in human ARVD/C, as CSN6 can complex with both DSP and PKP2 (Figure 1C). The *DSP R315C* mutation was of interest as it is an evolutionarily conserved amino acid within the DSP N-terminus (Figure 5C), a region that could directly interact with CSN6 (Figure 1). In addition, the *DSP R315C* variant alone has been identified in patient populations harboring a sudden death syndrome (26), which parallels disease consequences of ARVD/C (sudden death). Analyses of the high resolution crystal structure of human DSP (N-terminal) plakin domain revealed that R315 is buried between the interface of two α-helices where its charged sidechain stabilizes these adjacent α-helices (Figure 5D). Using *in silico* predictions, we showed that *DSP R315C* destabilizes the DSP plakin domain, by breaking the electrostatic network of side chains that tether adjacent α-helices (Figure 5D), which in turn, we hypothesized lead to a disruption of the DSP-CSN6 interaction. Forced yeast two-hybrid assays revealed that the *DSP R315C* mutation abrogated the interaction between DSP and CSN6 (Figure 5E), reinforcing *in silico* predictions and ability of this mutation to disrupt the DSP and CSN6 interaction. Consistent with these findings, CSN6 localization was lost at the cardiac cell junction in human ARVD/C heart harboring these same desmosomal mutations (Figure 5F). To further reinforce that destabilization of the desmosomal-CSN6 complex underlies human ARVD/C, we showcase findings from five autopsied ARVD/C hearts harboring classic desmosomal mutations (DSP and PKP2), that highlight reduced junctional localization of CSN6 as a recurrent molecular alteration observed in human ARVD/C hearts (Figure 6). N-cadherin (marker of fascia adherens

junction) junctional localization was not impacted in human ARVD/C hearts when compared to controls (Figure 6), further validating the specificity and relevance of junctional CSN6 dysregulation in human ARVD/C.

Loss of desmosomal proteome degradation control due to CSN6 loss is sufficient to trigger the desmosomal-targeted disease, ARVD/C. Kaplan–Meier survival analyses revealed premature death of adult *Csn6* knockout mice (Figure 7A and B). At late survival curve time points, *Csn6* knockout mice displayed grossly enlarged and dilated cardiac chambers (Figure 7C and D). Adult *Csn6* knockout mouse hearts also displayed extensive ventricular fibrosis and pronounced lipid deposition that was restricted to the myocardium and "triangle of dysplasia" (Figure 7E and F and Supplemental Figure 5A and B), reminiscent of pathological fibro-fatty infiltration found in human ARVD/C hearts (29). We further revealed biventricular dilatation, dysfunction and failure in adult *Csn6* knockout mouse hearts (Figure 7G and H and Supplemental Figure 5C), which is reminiscent of a biventricular form of human ARVD/C and given way to the recent adoption of the term arrhythmogenic cardiomyopathy to reference this class of diseases (30). At early survival curve time points, adult *Csn6* knockout hearts displayed preserved cardiac dimensions and function (Supplemental Figure 5D). Instead, electrocardiography tracings revealed the presence of frequent premature ectopic beats/arrhythmias as well as ventricular depolarization delay in *Csn6* knockout hearts (Figure 7I and J and Supplemental Figure 5E), reminiscent of early electrical defects found in human ARVD/C patients (8, 31). These data demonstrate the sufficiency of cardiac CSN6 loss to trigger classic electrical and structural features associated with human ARVD/C.

Human desmosomal mutations destabilizing CSN6 are sufficient to trigger the desmosomal targeted disease, ARVD/C. To precisely validate and extrapolate how desmosomal (compound) mutations found in the human ARVD/C patient impact CSN6 interactions and functions in an

independent adult heart setting, we generated compound heterozygous mice harboring the same human desmosomal mutations (Double Het, *Dsp R315C/+*; *Pkp2 IVS10-1 G>C/+*; Supplemental 6A-F). GST pull down assays exploiting GST-CSN6 and Double Het hearts extracts (for native DSP), highlighted the significant reduction of DSP binding to CSN6 in Double Het hearts (Figure 8A and B). These molecular alterations lead to a significant reduction in junctional CSN6 and desmosomal protein levels, including DSP and PKP2, as well as downstream targets, such as connexin43 in right ventricular cell-cell junction extracts from Double Het hearts when compared to controls (Figure 8C and E). Proteins found in non-desmosomal compartments (eg., N-cadherin, marks fascia adherens junction) were not significantly impacted in Double Het mouse (Figure 8C and E), highlighting specificity of junctional targets impacted by CSN6 loss. An impact on protein degradation pathways consistent with loss of CSN6 function was observed in Double Het hearts as a significant increase in neddylation (at the 80-88 kDa range) was observed when compared to controls (Figure 8D and E). Using cycloheximide chase assays, we also showed a significant and progressive reduction in the half-life of key desmosomal proteins (triggering their rapid degradation) in neonatal Double Het cardiomyocytes (Supplemental Fig. 6G and H), highlighting an early (neonatal) and specific impact of reduced junctional localization of CSN6 on desmosomal protein degradation in Double Het hearts. Adult Double Het mice exhibited classic features associated with ARVD/C, which also recapitulated disease features found in *Csn6* deficient mice. These included primary right ventricular defects (dilatation) (Figure 8F), in the absence of changes in left ventricular dimensions and function in Double Het hearts at an early age (Supplemental Figure 6I). Electrocardiography tracings also revealed the presence of frequent cardiac premature ectopic beats/arrhythmias in Double Het mice (Figure 8G). Electrical and functional deficits could be exacerbated with age in Double Het hearts as they exhibited evidence of recurrent baseline

arrhythmias associated with ventricular depolarization delay (QRS prolongation) as well as cardiac enlargement associated with left ventricular functional deficits (Figure 8H-K). Since we predicted that the *Dsp R315C* was sufficient on its own to destabilize interactions to CSN6, we also characterized single *Dsp R315C* homozygous mutant mice (*Dsp* Hom). GST pull down assays exploiting GST-CSN6 and *Dsp* Hom heart extracts (for native DSP), highlighted that these hearts now exhibited a complete abrogation in cardiac DSP binding to CSN6 (Supplemental Figure 7A). We show that deficits in these pathways were sufficient to trigger baseline electrical deficits (ventricular depolarization delay) and cardiac functional insufficiencies (reduced % fractional shortening) associated with ARVD/C in *Dsp* Hom mice (Supplemental Fig. 7B and D). Since exercise/catecholamines are known to exacerbate arrhythmias in ARVD/C (32, 33), we assessed arrhythmias in *Dsp* Hom mice in the context of isoproterenol (catecholamine) stress. We show that *Dsp* Hom mice exhibited a significant increase in catecholamine-induced arrhythmias when compared to controls (Supplemental Fig. 7C), further highlighting electrical deficits associated with ARVD/C. These data altogether highlight the importance of the DSP-CSN6 interaction (and their alterations in the context of classic human desmosomal mutations) as a trigger to the cardiac remodeling response associated with human ARVD/C in mice.

Discussion

We provide evidence for the presence of an enzymatically active CSN subcomplex (containing core subunits CSN5 and CSN6) at the cardiac desmosome that targets its degradation. We show that CSN6 is an integral component of the cardiac desmosomal complex tethered by a direct interaction with the N-terminus of DSP. Taking advantage of DSP and CSN6 crystal structures (16, 17), our studies revealed the minimal DSP-CSN6 binding interface, which occurs between the spectrin repeats in the N-terminus of DSP and the MPN-domain of CSN6. The MPN domain of CSN6 is required for de-neddylation activity as studies utilizing a fragment of CSN6 deleted of the MPN domain resulted in a 100 fold decrease in de-neddylation activity of the CSN complex (17). Further refinement of the minimal CSN subunits required for de-neddylation activity has identified the sufficiency and requirement of the CSN5-CSN6 heterodimer to trigger de-neddylation activity (17, 25). CSN5 is the only COP9 complex subunit that harbors enzymatic activity as a protease as its MPN domain contains an embedded JAB1 MPN domain metalloenzyme (JAMM) motif, which contains the required catalytic center to de-neddylate substrates (19, 34). We show that CSN5 is co-localized to cell junctions in the adult mouse heart, and its cell junction localization was dependent on the presence of CSN6, highlighting the presence of a minimal CSN subcomplex. *In vitro* studies have revealed that the CSN5-CSN6 heterodimer is sufficient to de-neddylate and facilitate cullin RING E3 ubiquitin ligase (CURLs) function (25), suggesting functional sufficiency of this minimal CSN subcomplex to enzymatically target substrates. Our studies highlight that CSN5-CSN6 likely heterodimerize at desmosomal junctions, but CSN5 may exclusively function to deneddylate CURLs and target desmosomal proteins for degradation. Future studies focused on disrupting the CSN5/6 heterodimer will be required to determine if CSN5 is also required for desmosomal substrate recognition.

The novelty of our studies lies in the identification of a desmosomal substrate recognition and protein turnover system imprinted within the desmosomal resident complex in the heart. The molecular architecture of the protein-protein interactions that define the desmosomal resident complex include desmosomal structural proteins, DSP (spectrin domain) and PKP2, which have a native affinity to the MPN domain of the core CSN member, CSN6 and thus, are recognized by neddylation-based protein degradation machinery. This concept is validated by our studies that show CSN6 interactions with desmosomal proteins, DSP and PKP2 in the adult mouse heart as well as the sufficiency of human desmosomal mutations in DSP and PKP2 to elicit reduction/abrogation of junctional localization of CSN6 in the adult mouse and human heart. CSN6's known interactions (heterodimerization) with CSN5, act to form a subcomplex at the desomosomal cell-cell junction to de-neddylate/inactivate specific CURLs (eg., cullin 3) to prevent desmosomal protein ubiquitination and degradation. This concept is validated in *Csn6* knockout hearts as they exhibit hyper-neddylated forms of select CURLs (cullins 1 and 3, which migrate at the 80-88 kDa range), further revealing CSN6 dependent cullins. We also show CURLs, such as cullin-3, are localized to cell-cell junctions, highlighting an epicenter in the cardiomyocyte that contains "enzymatically" functional COP9 machinery for de-neddylation activity. We speculate that CSN5's enriched expression at the cell-cell junction may also be the reason why global effects of CSN6 loss are not observed in other compartments of the cardiomyocyte, despite CSN6 residing in areas outside of the desmosome. MLN4924 (neddylation inhibitor) studies highlight the essential role of CSN6 in deneddylation functions as MLN4924 could alleviate the desmosomal protein loss caused by deletion/loss of CSN6. The CSN complex has been hypothesized to form a "holocomplex" containing all eight CSNs as well as smaller subcomplexes with a subset of CSNs such as CSN1/2/3/8 and CSN4/5/6/7 (35, 36). Our studies highlight enrichment of a subset of CSN

subunits to the cell-cell junction, as previous studies in the field utilizing cardiac-specific *Csn8* knockout mice highlight the absence of CSN8 localization to the cell-cell junction (20, 37). Future studies focused on dissecting whether other CSN members associate or functionally impact the desmosomal resident complex, will be required to identify the CSN6 subcomplex members and dynamics restraining desmosomal protein degradation in cardiomyocytes.

Our studies highlight that junctional reduction/loss of CSN6 is a central feature that drives derailed protein degradation and ARVD/C (diagnostic predictor of severity) in mice and man. We show using human myocardial tissue that reduced junctional localization of CSN6 is a molecular hallmark of ARVD/C associated with classic desmosomal mutations. We further show that cardiac *Csn6* knockout mice could recapitulate all classic disease features of ARVD/C. Central to these features is the loss of neddylation-mediated degradation control in *Csn6* knockout hearts, which triggered hyper-accumulation of ubiquitin and selective autophagy protein degradation machinery at the cardiac desmosome to target its structural destruction. The interplay between neddylation and ubiquitination in *Csn6* knockout hearts further highlight the sensitivity of the cardiomyocyte to stress associated with dysregulation of protein turnover pathways. Previous studies in cardiomyocytes showcase that disturbing the balance of COP9 function (by removing the complex subunit, CSN8) can in fact, lead to proteotoxicity (by overwhelming the ubiquitin proteasome system), which resulted in increased ubiquitination (20, 37). Our studies focused on deleting *Csn6* highlight similar consequences whereby cardiomyocyte CSN6 deficiency results in increased neddylation (increased CURL activity) in cell-cell junction fractions, leading to increases in ubiquitylation of substrate proteins that overwhelm the proteasome and autophagy system (eg., accumulation of autophagic structures) at this location, thus, resulting in increased/accumulation of ubiquitination. These results validate prior findings but give in addition, more mechanistic

insights into the interplay between neddylation and ubiquitination in cardiomyocytes. Interestingly, similar ultrastructural findings of accumulated protein degradation machinery at cell junctions has been reported in independent ARVD/C settings in mice and man (38, 39). Furthermore, we show that hearts from a classic ARVD/C mouse model (*Dsp*-cKO) displayed reduced junctional localization of CSN6 and similar protein degradation defects consistent with loss of CSN6 function. Finally we show the sufficiency of mice harboring human desmosomal mutations (Double Het, *Dsp* Hom) to destabilize junctional-associated CSN6 and trigger protein degradation defects (including triggering rapid desmosomal protein degradation) and cardiac disease (ARVD/C) features consistent with loss of CSN6 function. Interestingly, the rapid degradation of desmosomal proteins (reduced half-life of desmosomal proteins) observed in neonatal Double Het cardiomyocytes, further highlight the early disease consequences stemming from junctional reduction/loss of CSN6 in ARVD/C. Despite these findings, we cannot exclude the possibility that primary effects of desmosomal mutations contribute to ARVC disease causality in Double Het and *Dsp* Hom mice as opposed to CSN6 alone, given the complex nature of protein-protein interactions in the desmosomal resident complex and signalosome. Future studies focused on dissecting the impact of CSN6 functional restoration in Double Het and *Dsp* Hom mice will be required to determine whether ARVC disease causality is solely attributed to CSN6 loss in these models.

These studies set the stage to potentially reclassify desmosomal diseases, such as ARVD/C, as "diseases of desmosomal protein degradation" as well as provide mechanistic insights on new targets for intervention (deneddylation) for ARVD/C, which can be exploited to restore the whole desmosomal proteome in a setting where desmosomal variants can no longer bind proteins that are required to maintain their structure (eg., CSN6). We also identify compartmentalized functions for

subunits of a classically large protein degradation signalosome complex, like COP9, as well as the structural interface (spectrin-MPN domain interaction) of how CSNs may target select substrates. Studies in desmosomal mutant mice (Double Het; *Dsp* Hom) further reveal that the heart dysfunction and arrhythmias associated with CSN6 reduction, precisely showcases how dysregulated CSN6 pathways are integral to the progressive electrical and structural phenotypes found in ARVD/C patients with classic desmosomal mutations. More specifically we also highlight the impact of the *DSP R315C* variant alone or in combination with other variants to predisposing the heart to ARVD/C disease susceptibility and progression. Thus, the strength of our data comes from the use of a multi-pronged approach which combines data from five different genetic mouse models (*Dsp*-cKO, *Csn6*-iKO, *Csn6*-cKO, Double Het, *Dsp* Hom mutant) and human cardiac biopsies (harboring 6 distinct desmosomal mutations) alongside *in silico* data, which intervene with the CSN6-DSP interaction (in multiple ways), to provide evidence for a novel role for CSN6 in the mechanistic and pathological underpinnings of human ARVD/C.

The importance of maintaining desmosomal integrity is not only underscored in the human heart (resulting in ARVD/C) but also other organs such as kidney (resulting in polycystic kidney disease) and skin (resulting in palmoplantar keratodermas) as well as a variety of cancers (gastric, colorectal, prostate, bladder, breast, skin, head/neck, cervical, endometrial) and auto-immune diseases (pemphigus foliaceus & pemphigus vulgaris) (4, 7). We anticipate our findings have broad implications towards highlighting master regulatory mechanisms that are inherent to the desmosome, which may have implications in understanding drivers of other desmosomal-based diseases, such as cancers where desmosomal protein loss drives cancer metastasis progression (4). Since neddylation inhibitors are in phase 1 clinical trials to treat metastatic melanoma, acute myeloid leukemia and myelodysplastic syndromes (40, 41), our studies also provide new disease

indications and insights on sub-cellular targets of neddylation, which remain unclear in the field. Thus, our studies could also impact interpretations made from ongoing human clinical trials exploiting neddylation inhibitors as a therapeutic (40, 41).

Methods

Yeast-two-hybrid assays. Yeast-two-hybrid screens and forced yeast-two-hybrid assays were performed using the Matchmaker® Gold Yeast Two-Hybrid System (Clontech). For the yeast-two-hybrid screen, N-terminus DSP (1-519 amino acids) was cloned into pGBKT7 (bait plasmid) and transformed into the Y2HGold bait yeast strain (Clontech). Adult human heart cDNA library (Clontech Mate & Plate ^{TM} Library-Human Heart) served as prey and resided in a pGADT7 vector, which had been transformed into the Y187 yeast strain (Clontech). Mating and screening procedures were carried out as described by the manufacturer (Clontech). A very stringent cutoff for screening with fast growth on quadruple dropout plates was used for diploid yeast clones. After the screening, a total of 17 clones grew out. Colonies were further analyzed for active β-galactosidase using an X-Gal filter lift assay. Plasmids from blue-positive clones were isolated and sequenced. Eleven different genes were identified using BLAST analysis and 1 (strongest interaction) out of the 17 clones analyzed was *CSN6*. For forced yeast-2-hybrid assays, N-terminus *DSP* (WT or *R315C*) and *PKP2* (WT) were cloned into pGBKT7 (bait plasmid) and transformed into Y2HGold yeast strain, while full-length CSN6 was cloned into pGADT7 (prey plasmid) and transformed into the Y187 yeast strain. Mating (pGBKT7 constructs with pGADT7 constructs) was carried out (Clontech) and interactions were assessed by β-galactosidase activity according to manufacturer's instructions (Thermo Fisher). Negative controls (empty vector + CSN6; TD1 + CSN6) and positive (p53 + TD1) controls were used for β-galactosidase activity assays.

Molecular docking and mutational analysis. Structure information for human DSP (amino acids 179-625; RCSB PDB accession number: 3R6N) (16) and human COP9 subunit 6 (chain N in RCSB PDB accession number: 4D10) (17) was uploaded to ClusPro2.0 (https://cluspro.bu.edu/) for molecular in silico docking (42, 43). No restraints were put on the protein-protein docking

attempt. Resulting models should display a binding interface between the spectrin repeat encompassing R315 in DSP and the N-terminal MPN-domain in CSN6, as these were identified as minimal binding sites in our biochemical analyses. All models in the Van der Waals and electrostatic docking group matched these criteria. The model displaying the lowest energy score was further investigated (Figure 1B). For *in silico* modeling of the *R315C* mutation in *DSP*, structure minimization and calculation of energy changes (ΔΔG) was performed using YASARA and the FoldX module (44-46). The error margin of ΔΔG calculated by FoldX is approximately 0.5 kcal/mol, indicating that changes in that range are insignificant.

Experimental Animals. Cardiac-specific *Dsp* knockout have been previously generated and characterized (23). *Csn6* genomic DNA was isolated from 129-SV/J mouse genomic DNA library (Stratagene). The *Csn6* conditional targeting vector was designed to include loxP sites, surrounding pGKNeo cassette and exons 4-10 (Supplemental Figure 1A). G418-resistant embryonic stem cell (ES) clones were screened for homologous recombination by SpeI digestion, followed by Southern blot analysis, as previously described (47). A positive recombinant ES clone was microinjected into C57BL/6J blastocysts. Chimera mice were bred with C57BL/6J mice and crossed with *Sox2*-Cre mice (48) to selectively remove the pGKNeo cassette and generate *Csn6* floxed mice (*Csn6 flox/flox*). Cardiac-specific *Csn6* knockout mice (*Csn6*-cKO) were generated by crossing *Csn6 flox/flox* mice with a-myosin-heavy chain Cre (a-MHC-Cre) and cardiac inducible *Csn6* knockout mice (*Csn6*-iKO) were generated by crossing *Csn6 flox/flox* mice with a-MHC-MerCreMer (Supplemental Figure 1B) (21, 22). Six-week old *Csn6*-iKO and littermate controls were injected with tamoxifen (50mg/kg per day) intraperitoneally once a day for five consecutive days (Supplemental Figure 1C).

Mouse lines harboring heterozygous *Dsp R315C* mutation (*Dsp R315C/+*) and heterozygous *Pkp2 IVS10-1 G>C* mutation (*Pkp2 IVS10-1 G>C/+*) were generated using CRISPR-Cas9 mediated methods that have been previously described (49). Briefly, CRISPR guide RNAs and single-strand oligodeoxynucleotide templates (ssODNs) were designed for *Dsp R315C* and *Pkp2 IVS10-1 G>C* mutations (Supplemental Table 1). CRISPR RNAs were chemically synthesized to contain the guide RNAs for *Dsp R315C* and *Pkp2 IVS10-1 G>C* mutations (Supplemental Table 1). For *Dsp R315C* mutant mice, a mixture of *Dsp R315C* cRNA, ssODNs, trans-activating crRNA and commercially Cas9 protein was injected into pronuclei of one-cell stage zygotes from C57BL/6J mice (The Jackson Laboratory). For *Pkp2 IVS10-1 G>C* mutant mice, a mixture of *Pkp2 IVS10-1 G>C* cRNA, ssODNs, trans-activating crRNA and commercially Cas9 protein was injected into pronuclei of one-cell stage zygotes from C57BL/6J mice (The Jackson Laboratory). Genomic DNA was extracted from mouse tails and genomic fragments at target sites were amplified by PCR and sequencing. Genotype positive knockin mice were backcrossed with C57BL/6J mice (The Jackson Laboratory) for at least three generations to minimize for potential off-target effects. Double heterozygous (*Dsp R315C/+*; *Pkp2 IVS10-1 G>C/+*) mice were generated by crossing heterozygous *Dsp R315C* mutant mice with heterozygous *Pkp2 IVS10-1 G>C* mutant mice. *Dsp R315C* homozygous mutant mice were generated by crossing heterozygous *Dsp R315C* mutant mice.

Co-immunoprecipitation assays. Endogenous co-immunoprecipitation assays were performed as previously described (47). Adult mouse heart lysates were incubated overnight at 4°C with Protein G beads (GE Healthcare), which were pre-incubated with rabbit anti-CSN6 antibody (Enzolife, Cat#BML-PW8295) or control rabbit IgG (Sigma, Cat#I5006). Bound proteins were eluted followed by SDS-PAGE and immunodetection of desmoplakin (mouse, 1:1000, Bio-Rad,

Cat#2722-5204), plakophilin-2 (mouse, 1:1000, Fitzgerald, Cat#10R-P130b) and CSN6 (1:500, Enzolife, Cat#BML-PW8295).

Protein analysis. Total and insoluble (intercalated disc-enriched) protein extracts were isolated from cardiomyocytes and ventricles as previously described (23). Immunodetection of CSN6 (Rabbit, 1:1000, Enzolife, Cat#BML-PW8295), desmoplakin (mouse, 1:1000, Bio-Rad, Cat#2722-5204), desmoglein-2 (mouse, 1:300, Fitzgerald, Cat#10R-D106a), desmocollin-2 (rabbit, 1:500, Fitzgerald, Cat#20R-DR004), plakophilin-2 (mouse, 1:1000, Fitzgerald, Cat#10R-P130b), plakoglobin (goat, 1:1000, Sigma, Cat#SAB2500802), β-catenin (mouse, 1:1000, Cell signaling, Cat#8480), N-cadherin (rabbit, 1:1000, Abcam, Cat# ab76057), connexin 43 (rabbit, 1:1000, Invitrogen, Cat#71-0700), talin2 (mouse, 1:1000, Bio-Rad, Cat#MCA4771), vinculin (mouse, 1:1000, sigma, Cat#V9131), β1-integrin (rabbit, 1:1000, kind gift from R.S. Ross, University of California San Diego, La Jolla, CA, USA), NEDD8 (rabbit, 1:1000, Cell signaling, Cat#2745), ubiquitin (rabbit, 1:1000, Cell signaling, Cat#3933), p62 (guinea pig, 1:1000, Progen Biotechnik GMBH, Cat#71001), glyceraldehyde 3-phosphate dehydrogenase (mouse, 1:2000, Santa Cruz Biotechnology, Cat#sc32233), cullin1 (rabbit, 1:1000, sigma, Cat#C7117), cullin2 (rabbit, 1:1000, Thermo Fisher, Cat#51-1800), cullin 3 (Mouse, 1:1000, Santa Cruz Biotechnology, Cat#sc-166053), cullin4A (rabbit, 1:1000, Sigma, Cat#SAB1411512), cullin4B (rabbit, 1:1000, Abgent, Cat#AP20232c), β-actin (Mouse, 1:1000, Santa Cruz Biotechnology, Cat#sc47778), GST (Mouse, 1:1000, Thermo Fisher, Cat#MA4-004) and α-tubulin (mouse, 1:2000, Sigma, Cat#T9028) was performed as previously described (23).

Immunofluorescence microscopy. Heart cryosections were fixed in 100% acetone at -20ºC for 8 minutes and were blocked in 10% goat serum/ phosphate-buffered saline (PBS) before incubation with antibodies. Human myocardial paraffin sections were deparaffinized, rehydrated and heated

for antigen retrieval as previously described (50, 51). Sections were subsequently stained with primary antibodies against CSN6 (Goat, 1:100, Santa Cruz Biotechnology, Cat#sc-47965 or Rabbit, 1:100, Enzolife, Cat#BML-PW8295), desmoplakin (mouse, 1:1000, Bio-Rad, Cat#2722-5204), N-cadherin (rabbit, 1:100, Abcam, Cat#ab76057), CSN5 (rabbit, 1:100, cell signaling, Cat#6895S), plakoglobin (goat, 1:100, Sigma, Cat#SAB2500802), perilipin (rabbit, 1:100, Cell Signaling, Cat#3470S), cullin 3 (mouse, 1:100, Santa Cruz Biotechnology, Cat#sc-166053) and secondary antibodies (1:100, Jackson ImmunoResearch Inc.). Immuno-fluorescence images were acquired using confocal microscopy (Olympus FV1000 or Leica SP8).

Electron microscopy. Cardiac ventricles were processed for electron microscopy and images were captured with FEI Tecnai Spirit G2 BioTWIN Transmission Electron Microscope as previously described (23).

RNA isolation and real-time PCR analyses. Total RNA was isolated from hearts using TRIZOL (Invitrogen) according to the manufacturer's instructions. The first-strand cDNA was generated using PrimeScript RT Reagent Kit with gDNA Eraser (Takara). Real-time PCR was performed on heart cDNA using primer sequences (Supplemental Table 2) diluted in Power SYBR Green PCR master mix (Applied Biosystems) and using a Bio-Rad Mastercycler. All values were normalized to 18S and GAPDH mRNA levels.

Neonatal mouse ventricular cardiomyocyte isolation and treatments. Ventricular cardiomyocytes were isolated from neonatal (1–2 days old) mouse hearts and plated on laminin as previously described (23). Cardiomyocytes were subsequently infected with adenoviruses harboring lacZ (MOI 100) and Cre (MOI 100) for 24 hours and subsequently maintained in media consisting of DMEM, M199, 5% fetal bovine serum, 10% horse serum and 1% penicillin/streptomycin/ glutamine. For protein analyses, cardiomyocytes were collected at four days post-infection. For

cycloheximide (CHX) chase assays, *Csn6* floxed cardiomyocytes were infected with adenoviruses harboring lacZ (MOI 100) and Cre (MOI 100) for 48 hours, and treated with CHX (10 μg/ml) for 0, 8, 16, 24 and 32 hours and subjected to protein analysis. For cycloheximide chase assays in Double Het cardiomyocytes, neonatal mouse cardiomyocytes isolated from Double Het and WT mice were treated with CHX (10 μg/ml) for 0, 8, 16, 24, 36 and 48 hours and subjected to protein analysis. For MLN4924 treatment studies, cardiomyocytes were treated with 1μM MLN4924 or DMSO (vehicle) at 3 days post-infection and collected for protein analyses 6 hours later.

Human myocardial tissues. Myocardial section was generated from a cardiac biopsy (formalin-fixed, OCT embedded) from a patient harboring the *DSP R315C* and *PKP2 IVS10-1 G>C* mutation. This patient was referred to the Genetics of Cardiac Arrhythmia Program at University of California San Francisco and fulfilled revised clinical and diagnostic task force criteria for definite ARVD/C (52), upon comprehensive evaluation by cardiac magnetic resonance imaging, echocardiography, electrophysiology study and endomyocardial biopsy collection. Genetic testing on peripheral blood DNA was performed using a panel consisting of seven known ARVD/C genes (plakophilin-2, desmoplakin, desmoglein-2, desmocollin-2, plakoglobin, transmembrane protein 43, and ryanodine receptor-2) and using next generation sequencing. Non-ARVD/C heart tissue in Figure 5F was obtained from an explanted unused cadaveric donor heart at the time of organ donation, as the donor was not eligible for heart transplantation and their death was not cardiovascular related (San Diego, CA, USA). Myocardial sections (formalin-fixed, paraffin embedded) designated with mutations *DSP R1113X*, *DSP S1015fs1023X*, *DSP 1218+1G>A*, *PKP2 R413X* and *PKP2 V570fs576X* were obtained from autopsied hearts from sudden deaths with diagnosis of ARVD/C with mutations identified in first degree relatives and confirmed with genetic material from the deceased, as previously described (50, 51).

Histological analysis. Mouse hearts were perfused in a relaxation buffer consisting of 300 mM KCl in PBS and fixed with 4% paraformaldehyde. Fixed hearts were embedded in OCT tissue tek (Sakura) or dehydrated and embedded in paraffin as previously described (23). Sections were cut between 5 and 10 μm thickness. Whole-heart (5 μM) paraffin sections were stained with hematoxylin and eosin (Sigma-Aldrich) and Masson's trichrome (Sigma–Aldrich) stains according to the manufacturer's instructions. Whole-heart (10 μM) cryosections were stained with Oil Red O (Sigma–Aldrich) according to the manufacturer's instructions. Images were acquired with the Hamamatsu Nanozoomer 2.0 HT Slide Scanner.

Magnetic resonance imaging (MRI). In vivo cardiac MRI was performed on a 7T horizontal bore MR scanner (Bruker). A quadrature volume coil (Bruker) was used for RF signal transmission and a two-channel surface array coil (RAPID MRI) was used for reception of the RF signal. Cardiac CINE images were acquired with an IntraGate (Bruker) retrospective gated 2D gradient echo pulse sequence (FLASH) with the following parameters: TE=3.1 ms, TR=5.6 ms, flip angle= 7º, 300-400 repetitions and 20 frames. A field of view = 2.0 cm x 1.5 cm and data matrix =256 x 192 were prescribed for a spatial resolution = 0.078 mm/pixel. Equatorial frames containing the largest and smallest chamber diameters were selected to define the end-diastolic (ED) and end-systolic (ES) times, respectively. For MRI image analyses, two-dimensional (2D) endocardial contours were manually segmented for each heart at ED and ES (LV and RV) using image analysis software (Seg3D, NIH Center for Integrative Biomedical Computing). Contour areas were calculated with custom software in MATLAB, multiplied by the slice spacing and summed together to approximate calibrated end-diastolic volumes (EDV) and end-systolic volumes (ESV). Ejection fraction was defined as (EDV–ESV)/EDV x 100.

Echocardiography. Echocardiography was performed as previously described (47). Briefly, mice were anesthetized with 5% isoflurane for 15 seconds and maintained at 0.5% isoflurane during the procedure. VisualSonics, SonoSite FUJIFILM, Vevo 2100 ultrasound system with a linear transducer 32-56MHz (MS550S) was used to capture the images and videos. Measurements of heart rate, percentage fractional shortening (%FS) as well as left ventricular (LV) internal diameter at end-diastole (LVIDd) and end-systole (LVIDs) were determined from the M-mode tracing.

Surface and Telemetry ECG. Surface ECG was performed as previously described (23). Briefly, mice were anesthetized with 5% isoflurane for 15 seconds and maintained at 1.5% isoflurane during the procedure. Six needle electrodes (30 gauge) were inserted subcutaneously into right forearm and left leg. For isoproterenol treatment studies, baseline surface ECG recordings were obtained in mice. Mice were subsequently injected intraperitoneally with isoproterenol (2.5 mg/kg body weight) and then re-evaluated for surface ECG at 10-15 minutes post-injection. For conscious telemetry studies, ECG transmitters (DSI) were subcutaneously inserted into the backs of mice as described previously (23). Positive and negative leads were fixed to the right shoulder muscle and the left leg muscle, respectively. ECG data was continuously acquired for 48h following 1 week after recovery from the implantation. ECG data was analyzed using LabChart. Quantification of ectopic beats within ECG tracings was calculated during a 5-minute interval every hour for a total of five hours.

Protein expression and GST pulldown assay. GST pulldown assay was performed as previously described (53). Briefly, full length mouse *Csn6* was cloned into the pGEX-6P-1 vector (GE Life Sciences). GST-CSN6 and GST proteins were expressed in *E.coli* BL21 cells (Invitrogen; Life Technologies) and purified using Glutathione Sepharose 4B (GE Life Sciences). Protein concentration was determined through densitometry of Coomassie stained SDS-page gels. Hearts

were homogenized in lysis buffer (10mM Tris-HCl pH 8.0, 100 mM NaCl, 0.2% Nonidet P-40 and 1X protease and phosphatase inhibitors, 1mM DTT). Heart extracts (500 μg per tube) were incubated with approximately 5μg of GST or GST-CSN6 proteins on a rotator overnight at 4°C. Beads were washed three times with lysis buffer, resuspended in SDS-sample buffer. Bound proteins were analyzed through protein blot analyses.

Statistics. Data are presented in text and figures as mean values ± standard error of the mean. The sample size was defined by R software. alpha was set to 0.05 and power was 90% for all studies. GraphPad Prism was used for analyses and significance was evaluated by Student's two tailed t-test and one-way or two-way ANOVA following Tukey or Sidak multiple pairwise comparisons tests. For Kaplan-Meier survival analysis, significance was assessed by the log-rank test. A p value of <0.05 was considered statistically significant.

Study approval. All animal procedures were in full compliance with the guidelines approved by the University of California San Diego Animal Care and Use Committee. Procurement of ARVD/C human myocardial biopsy tissue was performed using standard procedures under protocols approved by institutional ethics review board at the University of California San Francisco (San Francisco, CA, USA). Consent for biopsy procedures and use of explanted tissues prospectively was obtained.

Author Contributions

F.S. conceived, designed and supervised experiments. F.S. and Y.L. wrote the manuscript. Y.L, R.C.L, T.I, S.L. and J.B. designed experiments. J.P. and R.C.L performed yeast-two-hybrid screen and forced yeast-two hybrid analyses, respectively. T.I and M.H.L generated and provided the *Csn6* targeting vector, respectively. R.C.L generated *Csn6* floxed mice, performed co-immunoprecipitation assays and immunofluorescence analyses on human ARVD/C heart tissue. Y.L. generated cardiac-specific *Csn6* knockout mouse lines and performed molecular, histological, cellular and ultrastructural studies as well as survival and electrophysiological analyses on *Csn6* knockout mouse lines as well as performed studies on *Dsp* knockout mice. S.L and J.B. provided advice and performed molecular docking studies. K.L.P. provided advice and supervised cardiac physiological studies. W.H.B and M.B. performed MRI and analyses of MRI images. N.D.D. performed echocardiography analyses. Y.G. performed telemetry studies. V.N. provided advice and use of non-ARVD/C heart tissue. M.S. and A.A. provided advice and use of heart tissue and genetics from ARVD/C patients.

Acknowledgments

We thank R.S. Ross (University of California-San Diego, La Jolla, CA, USA) for providing β1-integrin antibodies, W. Feng (University of California-San Diego) for assistance with sgRNA design and J. Blondelle (University of California-San Diego) for technical assistance. We are grateful for support from the Neuroscience Microscopy Shared Facility and the Cellular and Molecular Medicine Electron microscopy core facility at the University of California-San Diego. This work was supported by the (i) National Institutes of Health (NIH) National Heart Lung and Blood Institute grants HL142251 (F.S.), HL128457 (S.L.), HL095780 Diversity supplement (J.P.) and F31 predoctoral (HL120611) fellowship (J.P.), (ii) California Institute of Regenerative Medicine grant RB3-05103 (F.S., M.S.), (iii) Tobacco Related Disease Research Program grant 24RT-022 (F.S.), (iv) Department of Defense grant W81XWH1810380 (F.S.), (v) American Heart Association postdoctoral fellowships (Y.L., R.C.L) and (vi) National Science Foundation predoctoral fellowship (W.H.B). The University of California San Diego Neuroscience Microscopy Shared Facility is supported by a grant from the NIH (P30 NS047101). The electron micrographs were taken in the Cellular and Molecular Medicine Electron microscopy core facility, which is supported in part by National Institutes of Health Award number S10OD023527.

References

1. Su H, and Wang X. The ubiquitin-proteasome system in cardiac proteinopathy: a quality control perspective. *Cardiovascular research.* 2010;85(2):253-62.

2. Wang X, and Robbins J. Proteasomal and lysosomal protein degradation and heart disease. *J Mol Cell Cardiol.* 2014;71:16-24.

3. Lyon RC, Lange S, and Sheikh F. Breaking down protein degradation mechanisms in cardiac muscle. *Trends Mol Med.* 2013;19(4):239-49.

4. Najor NA. Desmosomes in Human Disease. *Annu Rev Pathol.* 2018;13:51-70.

5. Sheikh F, Ross RS, and Chen J. Cell-cell connection to cardiac disease. *Trends Cardiovasc Med.* 2009;19(6):182-90.

6. Vermij SH, Abriel H, and van Veen TA. Refining the molecular organization of the cardiac intercalated disc. *Cardiovasc Res.* 2017;113(3):259-75.

7. Dusek RL, and Attardi LD. Desmosomes: new perpetrators in tumour suppression. *Nat Rev Cancer.* 2011;11(5):317-23.

8. Delmar M, and McKenna WJ. The cardiac desmosome and arrhythmogenic cardiomyopathies: from gene to disease. *Circ Res.* 2010;107(6):700-14.

9. Vimalanathan AK, Ehler E, and Gehmlich K. Genetics of and pathogenic mechanisms in arrhythmogenic right ventricular cardiomyopathy. *Biophys Rev.* 2018;10(4):973-82.

10. Nepomnyashchikh LM, Lushnikova EL, and Semenov DE. Focal degradation of cytoplasmic organelles in cardiomyocytes during regenerative and plastic myocardial insufficiency. *Bulletin of experimental biology and medicine.* 2000;130(12):1190-5.

11. Lange S, Xiang F, Yakovenko A, Vihola A, Hackman P, Rostkova E, et al. The kinase domain of titin controls muscle gene expression and protein turnover. *Science.* 2005;308(5728):1599-603.

12. Hirschy A, Croquelois A, Perriard E, Schoenauer R, Agarkova I, Hoerstrup SP, et al. Stabilised beta-catenin in postnatal ventricular myocardium leads to dilated cardiomyopathy and premature death. *Basic research in cardiology.* 2010;105(5):597-608.

13. Hilenski LL, Terracio L, Haas AL, and Borg TK. Immunolocalization of ubiquitin conjugates at Z-bands and intercalated discs of rat cardiomyocytes in vitro and in vivo. *The journal of histochemistry and cytochemistry : official journal of the Histochemistry Society.* 1992;40(7):1037-42.

14. Balasubramanian S, Mani S, Shiraishi H, Johnston RK, Yamane K, Willey CD, et al. Enhanced ubiquitination of cytoskeletal proteins in pressure overloaded myocardium is accompanied by changes in specific E3 ligases. *Journal of molecular and cellular cardiology.* 2006;41(4):669-79.

15. Kapplinger JD, Landstrom AP, Salisbury BA, Callis TE, Pollevick GD, Tester DJ, et al. Distinguishing arrhythmogenic right ventricular cardiomyopathy/dysplasia-associated mutations from background genetic noise. *J Am Coll Cardiol.* 2011;57(23):2317-27.

16. Choi HJ, and Weis WI. Crystal structure of a rigid four-spectrin-repeat fragment of the human desmoplakin plakin domain. *J Mol Biol.* 2011;409(5):800-12.

17. Lingaraju GM, Bunker RD, Cavadini S, Hess D, Hassiepen U, Renatus M, et al. Crystal structure of the human COP9 signalosome. *Nature.* 2014;512(7513):161-5.

18. Milic J, Tian Y, and Bernhagen J. Role of the COP9 Signalosome (CSN) in Cardiovascular Diseases. *Biomolecules.* 2019;9(6).

19. Wei N, Serino G, and Deng XW. The COP9 signalosome: more than a protease. *Trends Biochem Sci.* 2008;33(12):592-600.

20. Su H, Li J, Menon S, Liu J, Kumarapeli AR, Wei N, et al. Perturbation of cullin deneddylation via conditional Csn8 ablation impairs the ubiquitin-proteasome system and causes cardiomyocyte necrosis and dilated cardiomyopathy in mice. *Circ Res.* 2011;108(1):40-50.

21. Abel ED, Kaulbach HC, Tian R, Hopkins JC, Duffy J, Doetschman T, et al. Cardiac hypertrophy with preserved contractile function after selective deletion of GLUT4 from the heart. *J Clin Invest.* 1999;104(12):1703-14.

22. Sohal DS, Nghiem M, Crackower MA, Witt SA, Kimball TR, Tymitz KM, et al. Temporally regulated and tissue-specific gene manipulations in the adult and embryonic heart using a tamoxifen-inducible Cre protein. *Circ Res.* 2001;89(1):20-5.

23. Lyon RC, Mezzano V, Wright AT, Pfeiffer E, Chuang J, Banares K, et al. Connexin defects underlie arrhythmogenic right ventricular cardiomyopathy in a novel mouse model. *Hum Mol Genet.* 2014;23(5):1134-50.

24. Cavadini S, Fischer ES, Bunker RD, Potenza A, Lingaraju GM, Goldie KN, et al. Cullin-RING ubiquitin E3 ligase regulation by the COP9 signalosome. *Nature.* 2016;531(7596):598-603.

25. Birol M, Enchev RI, Padilla A, Stengel F, Aebersold R, Betzi S, et al. Structural and biochemical characterization of the Cop9 signalosome CSN5/CSN6 heterodimer. *PLoS One.* 2014;9(8):e105688.

26. Zhao Q, Chen Y, Peng L, Gao R, Liu N, Jiang P, et al. Identification of rare variants of DSP gene in sudden unexplained nocturnal death syndrome in the southern Chinese Han population. *Int J Legal Med.* 2016;130(2):317-22.

27. Groeneweg JA, Ummels A, Mulder M, Bikker H, van der Smagt JJ, van Mil AM, et al. Functional assessment of potential splice site variants in arrhythmogenic right ventricular dysplasia/cardiomyopathy. *Heart Rhythm.* 2014;11(11):2010-7.

28. Svensson A, Astrom-Aneq M, Widlund KF, Fluur C, Green A, Rehnberg M, et al. Arrhythmogenic Right Ventricular Cardiomyopathy - 4 Swedish families with an associated PKP2 c.2146-1G>C variant. *Am J Cardiovasc Dis.* 2016;6(2):55-65.

29. Thiene G, Corrado D, and Basso C. Arrhythmogenic right ventricular cardiomyopathy/dysplasia. *Orphanet J Rare Dis.* 2007;2:45.

30. Sen-Chowdhry S, Syrris P, Ward D, Asimaki A, Sevdalis E, and McKenna WJ. Clinical and genetic characterization of families with arrhythmogenic right ventricular dysplasia/cardiomyopathy provides novel insights into patterns of disease expression. *Circulation.* 2007;115(13):1710-20.

31. Quarta G, Muir A, Pantazis A, Syrris P, Gehmlich K, Garcia-Pavia P, et al. Familial evaluation in arrhythmogenic right ventricular cardiomyopathy: impact of genetics and revised task force criteria. *Circulation.* 2011;123(23):2701-9.

32. Denis A, Sacher F, Derval N, Martin R, Lim HS, Pambrun T, et al. Arrhythmogenic response to isoproterenol testing vs. exercise testing in arrhythmogenic right ventricular cardiomyopathy patients. *Europace.* 2018;20(FI1):f30-f6.

33. Denis A, Sacher F, Derval N, Lim HS, Cochet H, Shah AJ, et al. Diagnostic value of isoproterenol testing in arrhythmogenic right ventricular cardiomyopathy. *Circ Arrhythm Electrophysiol.* 2014;7(4):590-7.

34. Cope GA, Suh GS, Aravind L, Schwarz SE, Zipursky SL, Koonin EV, et al. Role of predicted metalloprotease motif of Jab1/Csn5 in cleavage of Nedd8 from Cul1. *Science.* 2002;298(5593):608-11.

35. Sharon M, Mao H, Boeri Erba E, Stephens E, Zheng N, and Robinson CV. Symmetrical modularity of the COP9 signalosome complex suggests its multifunctionality. *Structure.* 2009;17(1):31-40.

36. Kotiguda GG, Weinberg D, Dessau M, Salvi C, Serino G, Chamovitz DA, et al. The organization of a CSN5-containing subcomplex of the COP9 signalosome. *The Journal of biological chemistry.* 2012;287(50):42031-41.

37. Su H, Li J, Osinska H, Li F, Robbins J, Liu J, et al. The COP9 signalosome is required for autophagy, proteasome-mediated proteolysis, and cardiomyocyte survival in adult mice. *Circ Heart Fail.* 2013;6(5):1049-57.

38. Kant S, Krull P, Eisner S, Leube RE, and Krusche CA. Histological and ultrastructural abnormalities in murine desmoglein 2-mutant hearts. *Cell Tissue Res.* 2012;348(2):249-59.

39. Te Rijdt WP, van Tintelen JP, Vink A, van der Wal AC, de Boer RA, van den Berg MP, et al. Phospholamban p.Arg14del cardiomyopathy is characterized by phospholamban aggregates, aggresomes, and autophagic degradation. *Histopathology.* 2016;69(4):542-50.

40. Bhatia S, Pavlick AC, Boasberg P, Thompson JA, Mulligan G, Pickard MD, et al. A phase I study of the investigational NEDD8-activating enzyme inhibitor pevonedistat (TAK-924/MLN4924) in patients with metastatic melanoma. *Invest New Drugs.* 2016;34(4):439-49.

41. Swords RT, Erba HP, DeAngelo DJ, Bixby DL, Altman JK, Maris M, et al. Pevonedistat (MLN4924), a First-in-Class NEDD8-activating enzyme inhibitor, in patients with acute myeloid leukaemia and myelodysplastic syndromes: a phase 1 study. *Br J Haematol.* 2015;169(4):534-43.

42. Comeau SR, Gatchell DW, Vajda S, and Camacho CJ. ClusPro: a fully automated algorithm for protein-protein docking. *Nucleic Acids Res.* 2004;32(Web Server issue):W96-9.

43. Kozakov D, Hall DR, Xia B, Porter KA, Padhorny D, Yueh C, et al. The ClusPro web server for protein-protein docking. *Nat Protoc.* 2017;12(2):255-78.

44. Land H, and Humble MS. YASARA: A Tool to Obtain Structural Guidance in Biocatalytic Investigations. *Methods Mol Biol.* 2018;1685:43-67.

45. Schymkowitz J, Borg J, Stricher F, Nys R, Rousseau F, and Serrano L. The FoldX web server: an online force field. *Nucleic Acids Res.* 2005;33(Web Server issue):W382-8.

46. Van Durme J, Delgado J, Stricher F, Serrano L, Schymkowitz J, and Rousseau F. A graphical interface for the FoldX forcefield. *Bioinformatics.* 2011;27(12):1711-2.

47. Sheikh F, Raskin A, Chu PH, Lange S, Domenighetti AA, Zheng M, et al. An FHL1-containing complex within the cardiomyocyte sarcomere mediates hypertrophic biomechanical stress responses in mice. *J Clin Invest.* 2008;118(12):3870-80.

48. Hayashi S, Lewis P, Pevny L, and McMahon AP. Efficient gene modulation in mouse epiblast using a Sox2Cre transgenic mouse strain. *Gene Expr Patterns.* 2002;2(1-2):93-7.

49. Ma X, Chen C, Veevers J, Zhou X, Ross RS, Feng W, et al. CRISPR/Cas9-mediated gene manipulation to create single-amino-acid-substituted and floxed mice with a cloning-free method. *Sci Rep.* 2017;7:42244.

50. Asimaki A, Tandri H, Huang H, Halushka MK, Gautam S, Basso C, et al. A new diagnostic test for arrhythmogenic right ventricular cardiomyopathy. *N Engl J Med.* 2009;360(11):1075-84.

51. Syrris P, Ward D, Asimaki A, Sen-Chowdhry S, Ebrahim HY, Evans A, et al. Clinical expression of plakophilin-2 mutations in familial arrhythmogenic right ventricular cardiomyopathy. *Circulation.* 2006;113(3):356-64.

52. Marcus FI, McKenna WJ, Sherrill D, Basso C, Bauce B, Bluemke DA, et al. Diagnosis of arrhythmogenic right ventricular cardiomyopathy/dysplasia: proposed modification of the Task Force Criteria. *Eur Heart J.* 2010;31(7):806-14.

53. Lange S, Gehmlich K, Lun AS, Blondelle J, Hooper C, Dalton ND, et al. MLP and CARP are linked to chronic PKCalpha signalling in dilated cardiomyopathy. *Nat Commun.* 2016;7:12120.

Figure 1

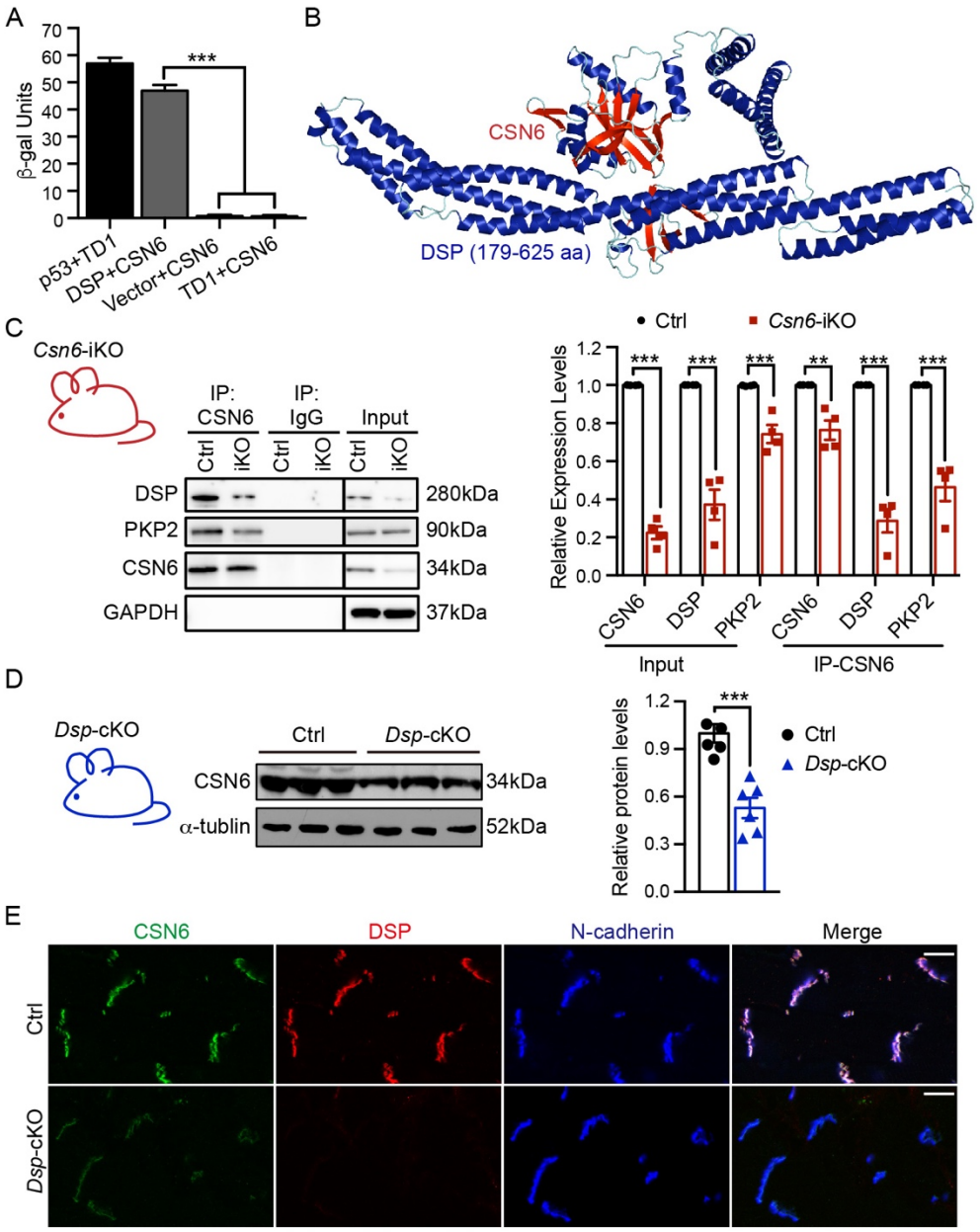

Figure 1: Identification of CSN6 as a novel cardiac desmosomal interacting protein. (**A**) Quantitative β-galactosidase activity assays from forced yeast-2-hybrid studies. p53 with TD1 served as positive control. Vector with CSN6 and TD1 with CSN6 served as negative controls. Data are mean ± s.e.m; one-way ANOVA with Tukey's multiple comparisons test, ***P<0.001. (**B**) *In silico* molecular docking of full-length CSN6 (Red) and DSP N-terminus (amino acids 179-625, Blue) was performed using ClusPro. Resulting models displayed a binding interface between the spectrin repeat encompassing R315 in desmoplakin (DSP) and the N-terminal MPN-domain

in CSN6, as these were identified as minimal binding sites in our biochemical analyses. (**C**) CSN6 was immunoprecipitated from control (Ctrl) and *Csn6*-inducible KO (iKO) mouse heart extracts at 10 weeks of age and subjected to protein blot analyses and quantification for DSP, plakophilin-2 (PKP2) and CSN6 protein levels as indicated (n=4 per group). IgG serum was used as a control. Input refers to total protein prior to co-immunoprecipitation assay. Relative expression of input proteins were normalized to the loading control GAPDH. Data are mean ± s.e.m; two-way ANOVA with Sidak multiple comparison test, $^{**}P<0.01$, $^{***}P<0.001$. Molecular weight standards are indicated. (**D**) Protein blot analysis and quantification of CSN6 protein levels in insoluble heart extracts from *Dsp*-cKO and control mice (n=6 per group). The relative expression level of CSN6 was normalized to the loading control α-tubulin. Data are mean ± s.e.m; Student's two-tailed t-test, $^{***}P<0.001$. Molecular weight standards are indicated. (**E**) Immunofluorescence staining of DSP (red), CSN6 (green) and N-cadherin (blue) in *Dsp*-cKO and control mouse heart sections (n=3 per group). Scale bar: 10μm.

Figure 2

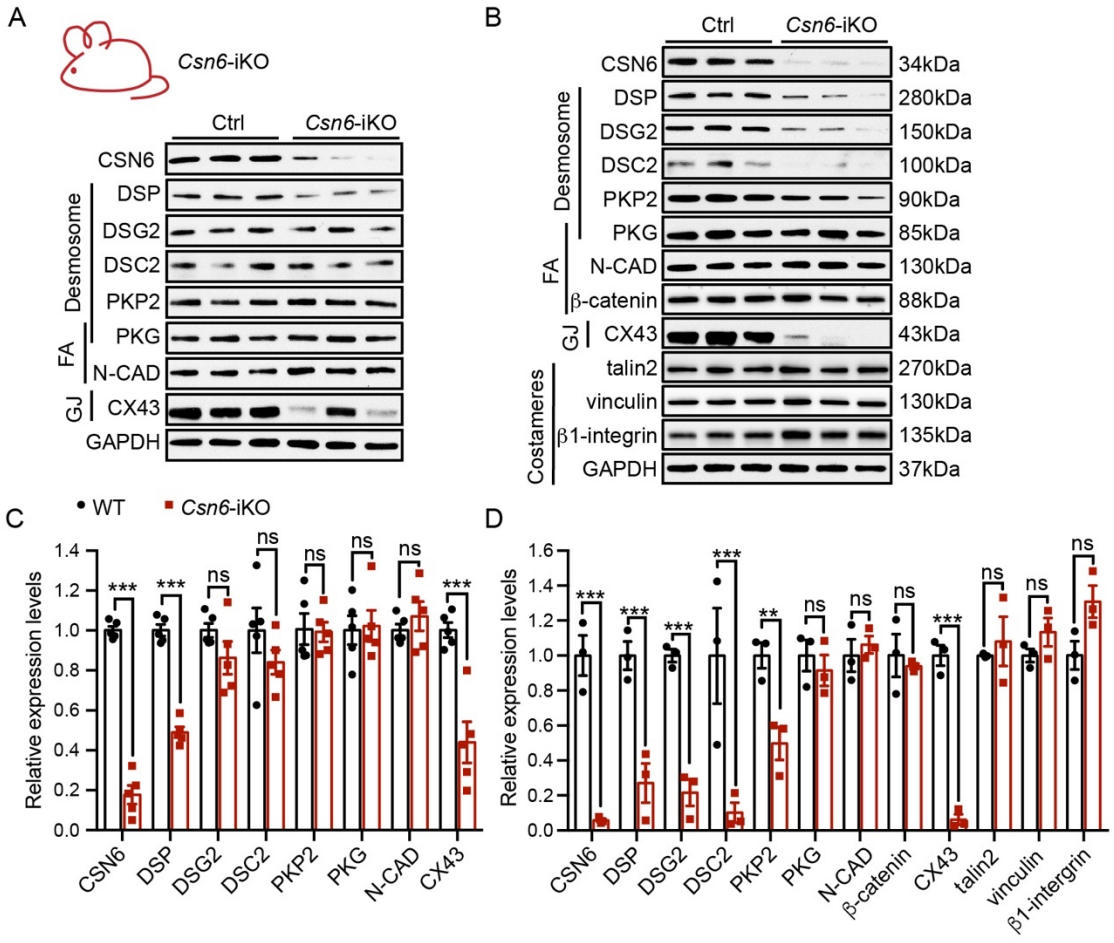

Figure 2: Cardiac CSN6 loss accelerated desmosomal protein dissolution *in vivo*. (**A** and **C**) Protein blot analyses (**A**) and quantification of protein expression levels (**C**) in total protein extracts from *Csn6*-iKO and control hearts at 2 weeks post tamoxifen injection (n=5 per group). (**B** and **D**) Protein blot analyses (**B**) and quantification of protein expression levels (**D**) in total protein extracts from *Csn6*-iKO and control hearts at 6 weeks post tamoxifen injection (n=3 per group). FA: fascia adherens. GJ: gap junction. The expression levels of proteins were normalized to the loading control GAPDH. Data are mean ± s.e.m; two-way ANOVA with Sidak multiple comparison test, **P*<0.05, ***P*<0.01, ****P*<0.001, ns, not significant.

Figure 3

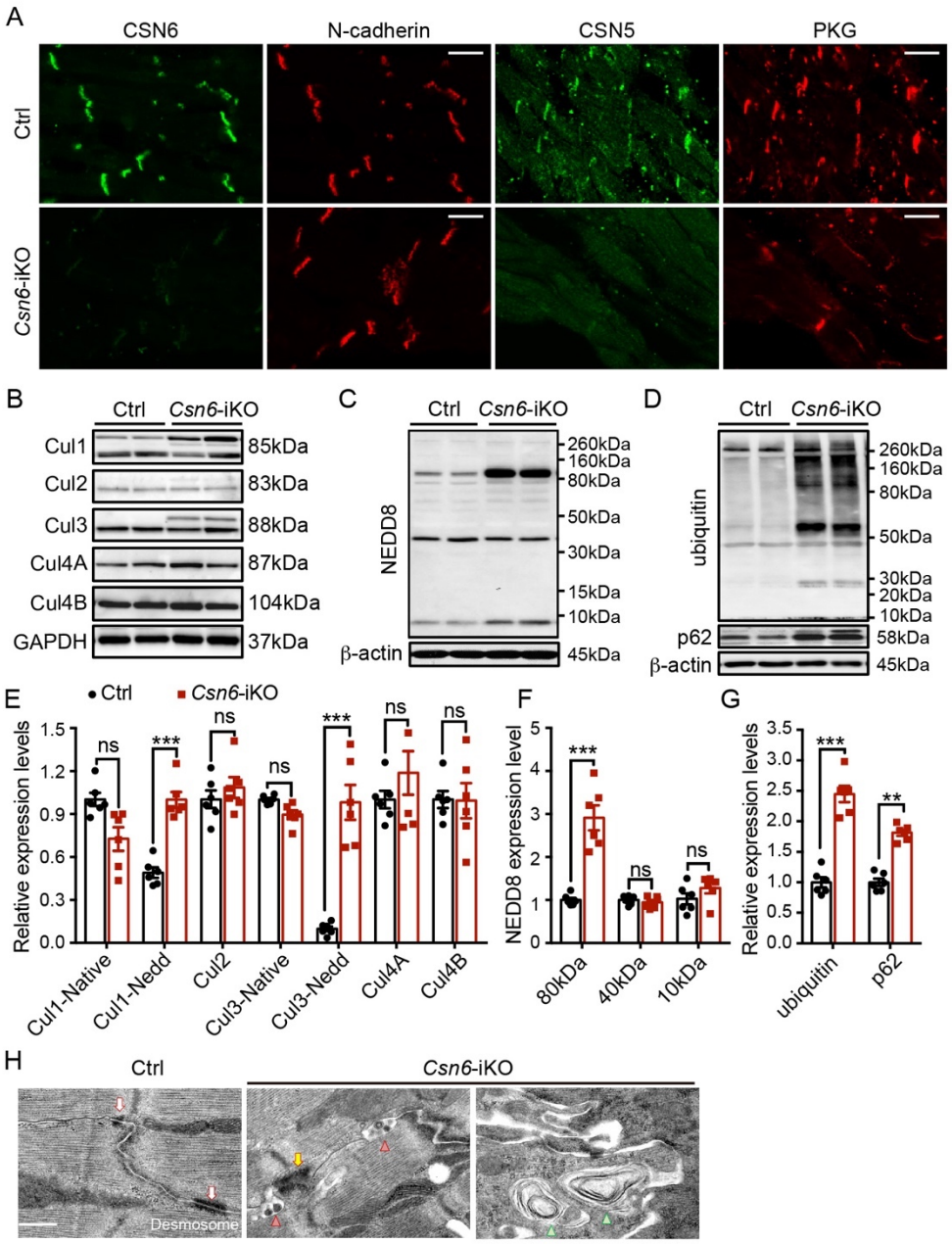

Figure 3: Neddylation-mediated protein degradation is impacted by CSN6 loss. (**A**) Immunofluorescence staining of CSN subunits (CSN6 and CSN5, green) and cell-cell junctional marker (N-cadherin or PKG, red) in heart sections from *Csn6*-iKO and control mice at 2 weeks post tamoxifen injection (n=3 per group). Bar represents 20 μm. (**B-D**) Protein blot analyses of cullin E3 ligases (**B**), NEDD8 (**C**), ubiquitin and p62 levels (**D**) in ventricular extracts from *Csn6*-iKO and control mice at 6 weeks post tamoxifen injection (n=6 per group). (**E-G**) Quantification

of protein expression levels in (**B-D**), respectively. The expression levels of proteins were normalized to the loading control GAPDH or β-actin. Data are mean ± s.e.m; two-way ANOVA with Sidak multiple comparison test, ***P<0.001, ns, not significant. (**H**) Representative transmission electron micrographs from the right ventricle of *Csn6*-iKO and littermate control (n=4 per group). White arrows denote desmosome. Yellow arrows denote disorganized desmosome. Red arrowheads denote autophagic vacuoles. Green arrowheads denote multi-membraned "autophagic-like" vesicles. Bar represents 500 nm.

Figure 4

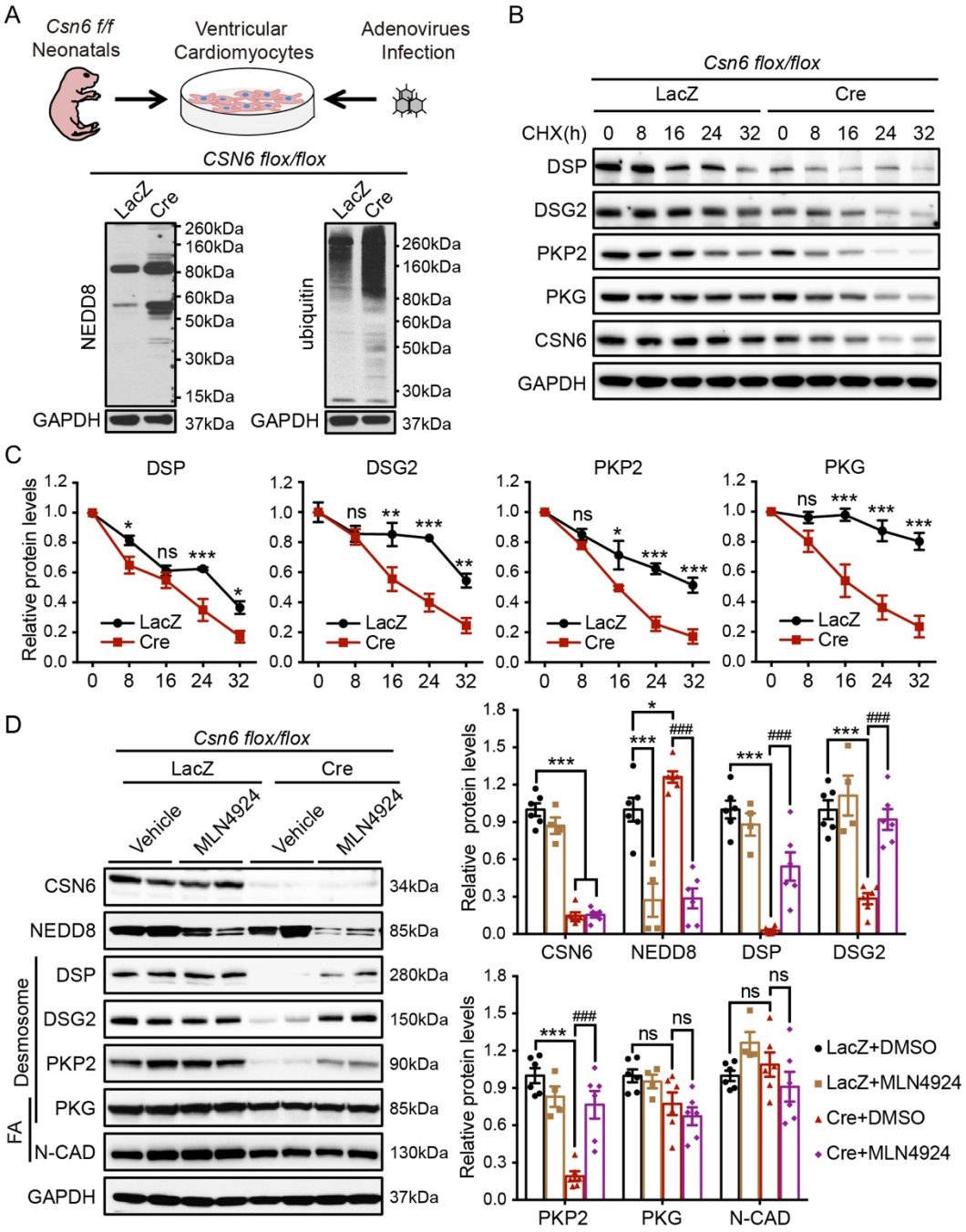

Figure 4: CSN6-mediated protein degradation pathway targets desmosomal proteome degradation. (**A**) Protein blot analyses of Nedd8 and ubiquitin levels in *Csn6* deficient (Cre, MOI 100) and control (lacZ, MOI 100) ventricular cardiomyocytes. Experiments were repeated independently three times (2 wells per condition) with similar results. (**B** and **C**) Representative protein blots (**B**) and quantification analyses (**C**) of desmosomal proteins in *Csn6* deficient (Cre,

MOI 100) and control (lacZ, MOI 100) ventricular cardiomyocytes. After 48 hour infection, cardiomyocytes were treated with cycloheximide (CHX, 10 μg/ml) for 0, 8, 16, 24 and 32 hours. The expression levels of proteins were normalized to the loading control GAPDH. Data are mean ± s.e.m; two-way ANOVA with Sidak multiple comparison test, **P*<0.05, ***P*<0.01, ****P*<0.001, ns, not significant. (**D**) Protein blot analyses and quantification of protein expression levels of cell-cell junction proteins and NEDD8 levels in *Csn*6 deficient (Cre, MOI 100) and control (lacZ, MOI 100) ventricular cardiomyocytes in the presence of vehicle or MLN4924 treatment. The expression levels of proteins were normalized to the loading control GAPDH. Data are mean ± s.e.m; two-way ANOVA with Sidak multiple comparison test, **P*<0.05, ****P*<0.001, when compared to the control cardiomyocytes treated with DMSO (LacZ+DMSO). ###*P*<0.001, when compared to the *Csn6* deficient cardiomyocytes treated with DMSO (Cre+DMSO). ns, not significant. Experiments were repeated independently three times (2 wells per condition) with similar results.

Figure 5

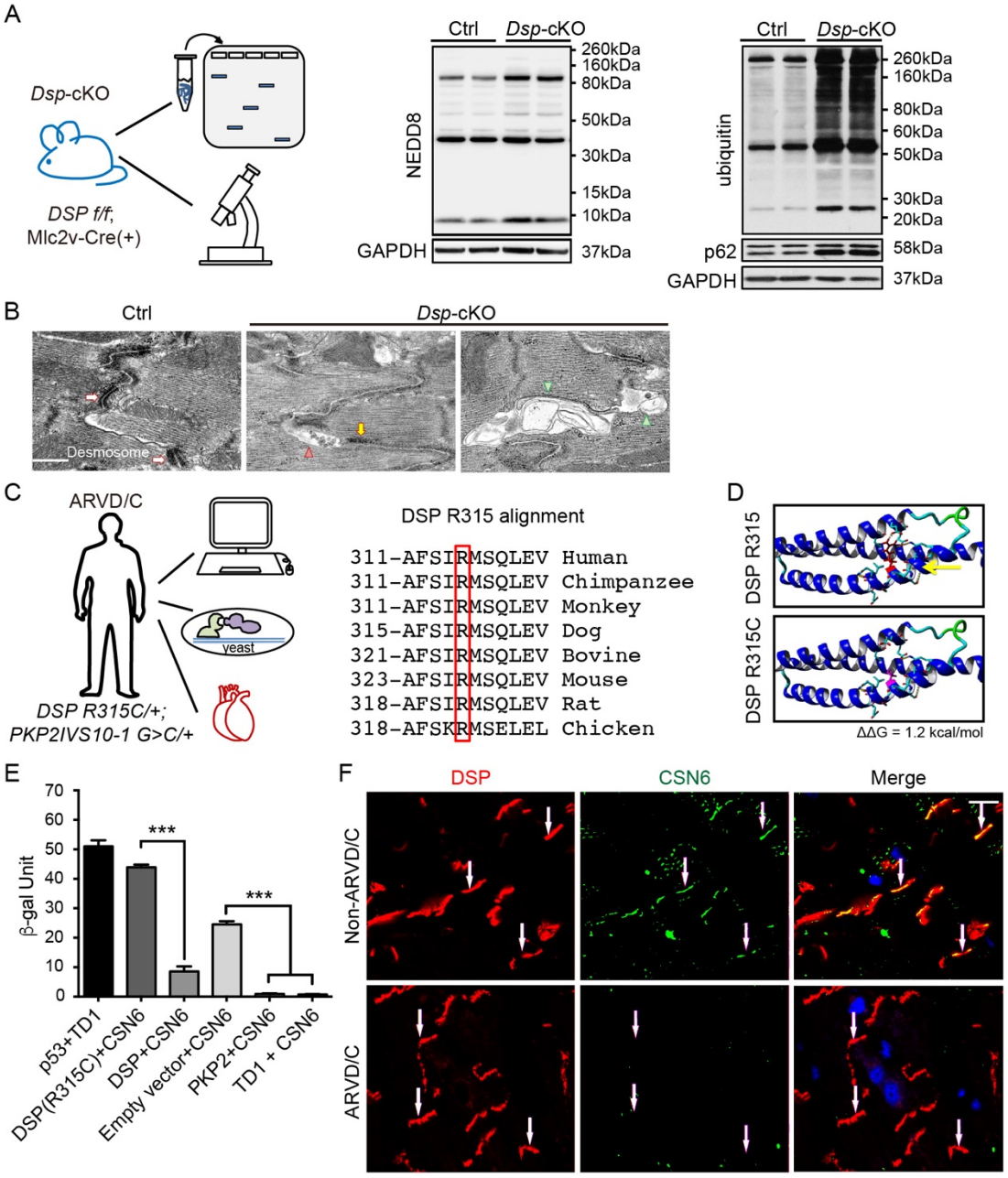

Figure 5: Disruption of the CSN6-desmosomal complex and protein degradation pathways underlies ARVD/C in mice and man. (**A**) Protein blot analysis of NEDD8, ubiquitin and p62 levels in ventricular extracts from *Dsp*-cKO and control mice at 8 weeks of age (n=5-6 per group). (**B**) Representative transmission electron micrographs from the right ventricle of *Dsp*-cKO and littermate control (n=4 per group). White arrows denote desmosome. Yellow arrows denote disorganized desmosome. Red arrowheads denote autophagic vacuoles. Green arrowheads denote

multi-membraned “autophagic-like” vesicles. Bar represents 500 nm. (**C**) DSP R315 region sequence alignment across vertebrate species. Red square denotes R315. (**D**) *In silico* molecular docking studies of DSP R315 (top) and R315C mutation (bottom). ΔΔG (change from R315 to R315C) is predicted with FoldX. ΔΔG > 0 = destabilizing and ΔΔG < 0= stabilizing. (**E**) β-galactosidase activity from forced yeast-2-hybrid studies. p53 with TD1 served as a positive control. Vector with CSN6 and TD1 with CSN6 served as negative controls. Data are mean ± s.e.m; one-way ANOVA with Tukey's multiple comparisons test, ***P<0.001. Experiments were repeated independently three times with similar results. (**F**) Immunofluorescence staining of DSP (red) and CSN6 (green) in heart biopsies from an ARVD/C patient (harboring *DSP R315C* and *PKP2 IVS10-1 G>C* mutations) and non-ARVC control. White arrows denote cell-cell junction. Bar represents 10 μm.

Figure 6

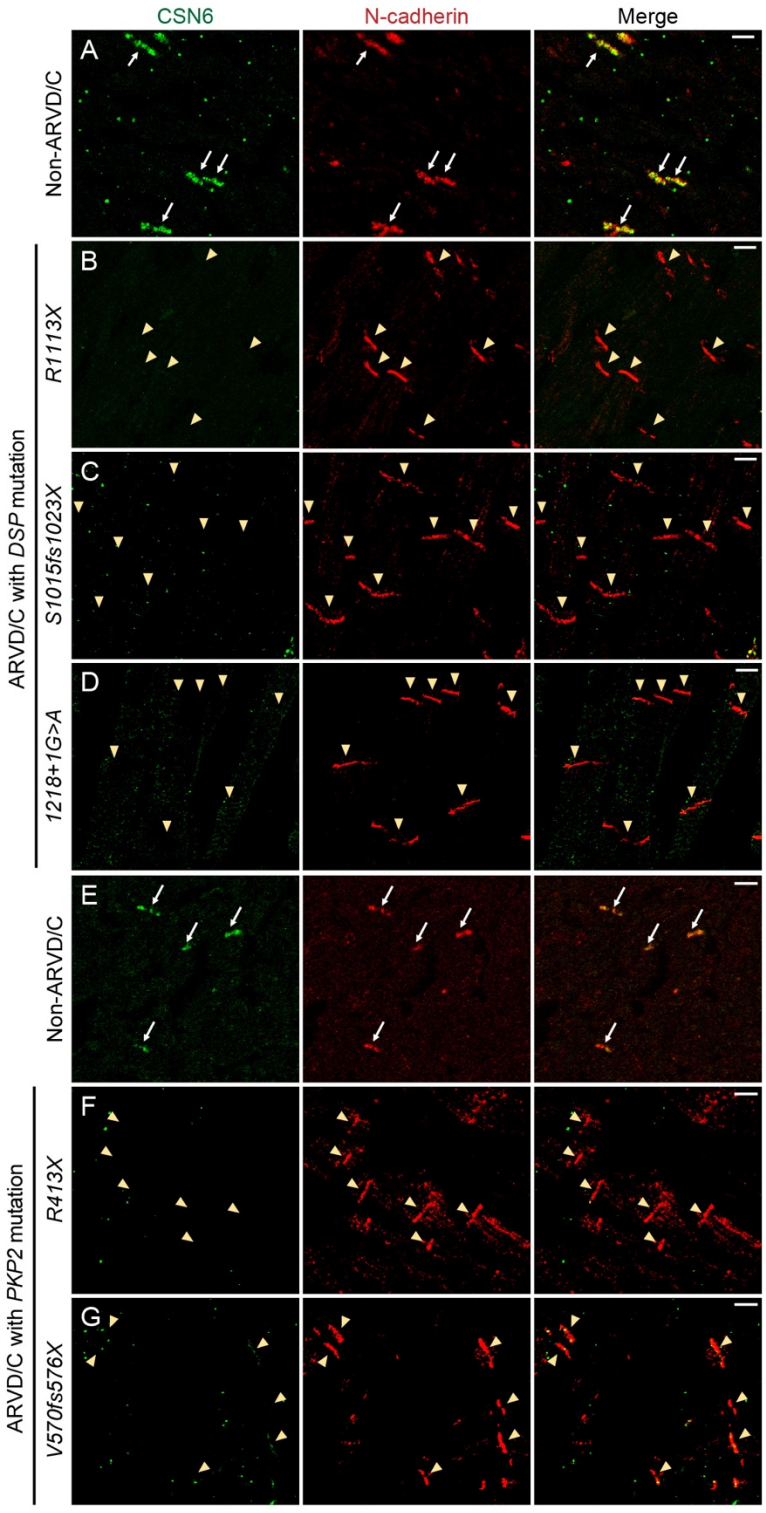

Figure 6: Human desmosomal mutations associated with ARVD/C impact CSN6 localization. (**A-G**) Immunofluorescence staining of N-cadherin (red) and CSN6 (green) in ARVD/C heart

autopsies harboring *DSP* or *PKP2* mutation and non-ARVD/C control. White arrows denote the cell-cell junctions which express both CSN6 and N-cadherin. Yellow arrowheads denote the cell-cell junctions which only express N-cadherin. Bar represents 10 μm.

Figure 7

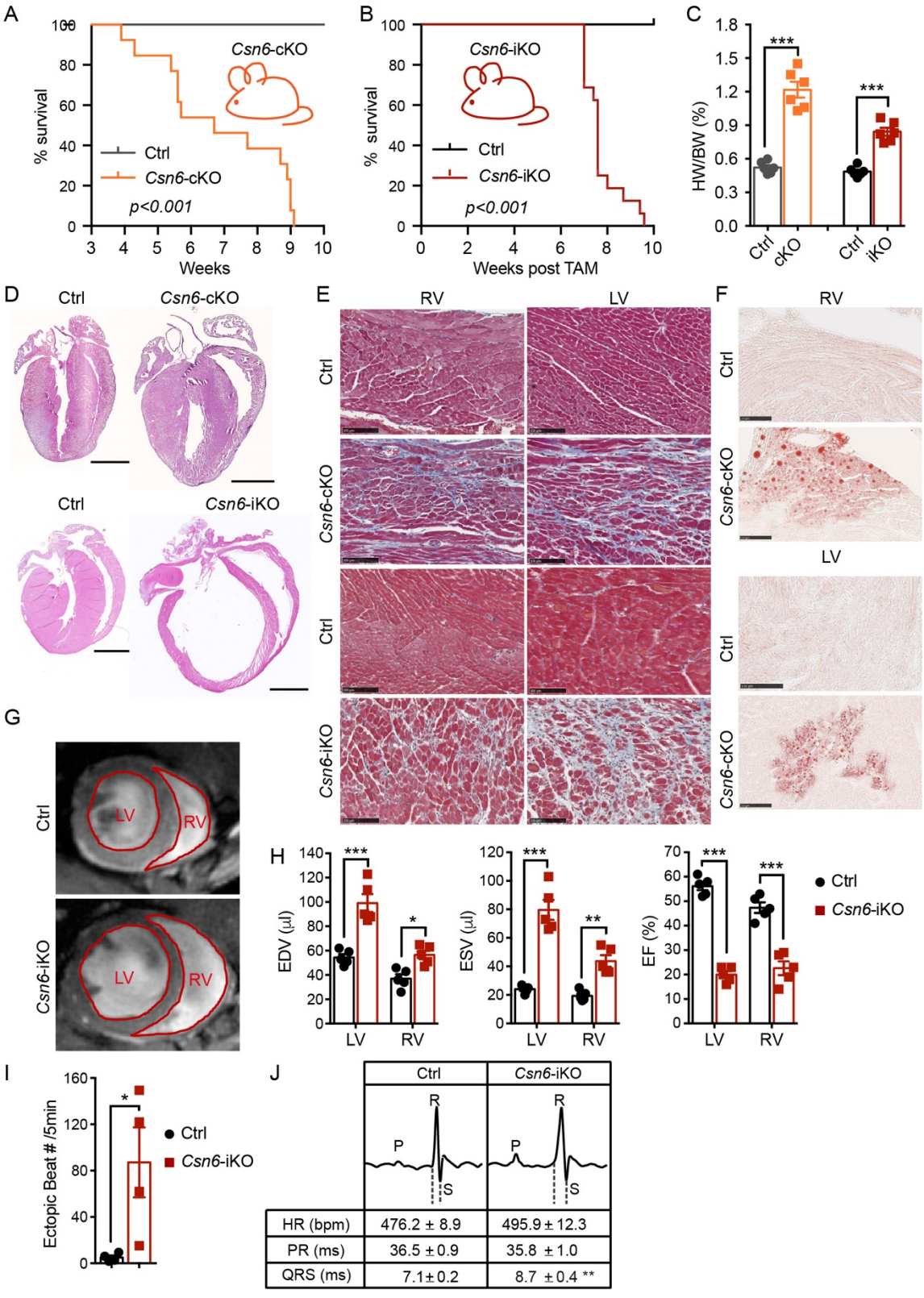

	Ctrl	*Csn6*-iKO
HR (bpm)	476.2 ± 8.9	495.9 ± 12.3
PR (ms)	36.5 ± 0.9	35.8 ± 1.0
QRS (ms)	7.1 ± 0.2	8.7 ± 0.4 **

Figure 7: Cardiac specific loss of CSN6 in mice results in sudden death and recapitulates key disease features of ARVD/C. (**A** and **B**) Kaplan–Meier survival curve analysis of *Csn6*-cKO and control (**A**, n=13) as well as *Csn6*-iKO and control (**B**, n=16) mice post tamoxifen injection (log-rank test). (**C**) Heart weight to body weight ratios (HW/BW) from control and *Csn6* deficient mice (n=6 per group). Data are mean ± s.e.m; two-way ANOVA with Sidak multiple comparison test). ***P<0.001. (**D**) Representative whole heart sections from *Csn6* deficient and control mice at 6 weeks of age or post-tamoxifen injection (n=4 per group). Sections were stained for nuclei and cytoplasm with hematoxylin and eosin, respectively. Scale bar: 2mm. (**E**) Representative Masson's trichrome stained cardiac sections from *Csn6* deficient and control mice at 6 weeks of age or post-tamoxifen injection (n=4 per group). Scale bar: 100μm. (**F**) Representative Oil Red O stained cardiac sections from *Csn6*-cKO and control mice at 6 weeks of age (n=4 per group). Scale bar: 50μm. (**G**) Representative magnetic resonance images (short axis) from control and *Csn6*-iKO hearts at 6 weeks post-tamoxifen injection (n=5 per group). (**H**) MRI analyses of left and right ventricular ejection fractions (EF), end-diastolic volume (EDV) and end-systolic volume (ESV) in control and *Csn6*-iKO hearts at 6 weeks post-tamoxifen injection. Data are mean ± s.e.m; two-way ANOVA with Sidak multiple comparison test, **P<0.01, ***P<0.001. (**I**) Quantification of number of ectopic beats in *Csn6*-iKO and control mice (n=4 per group) at 2 weeks post-tamoxifen injection. Data are mean ± s.e.m; Student's two-tailed t-test. *P<0.05. (**J**) Representative surface ECG tracings in *Csn6*-iKO and control mice at 2 weeks post-tamoxifen injection (n=10 per group). Quantification of heart rate (HR), PR and QRS intervals from ECG tracings was performed. Data from 100 ECG tracings per mouse were averaged for analysis. Data are mean ± s.e.m; Student's two-tailed t-test, **P<0.01. QRS duration is indicated by the dotted line.

Figure 8

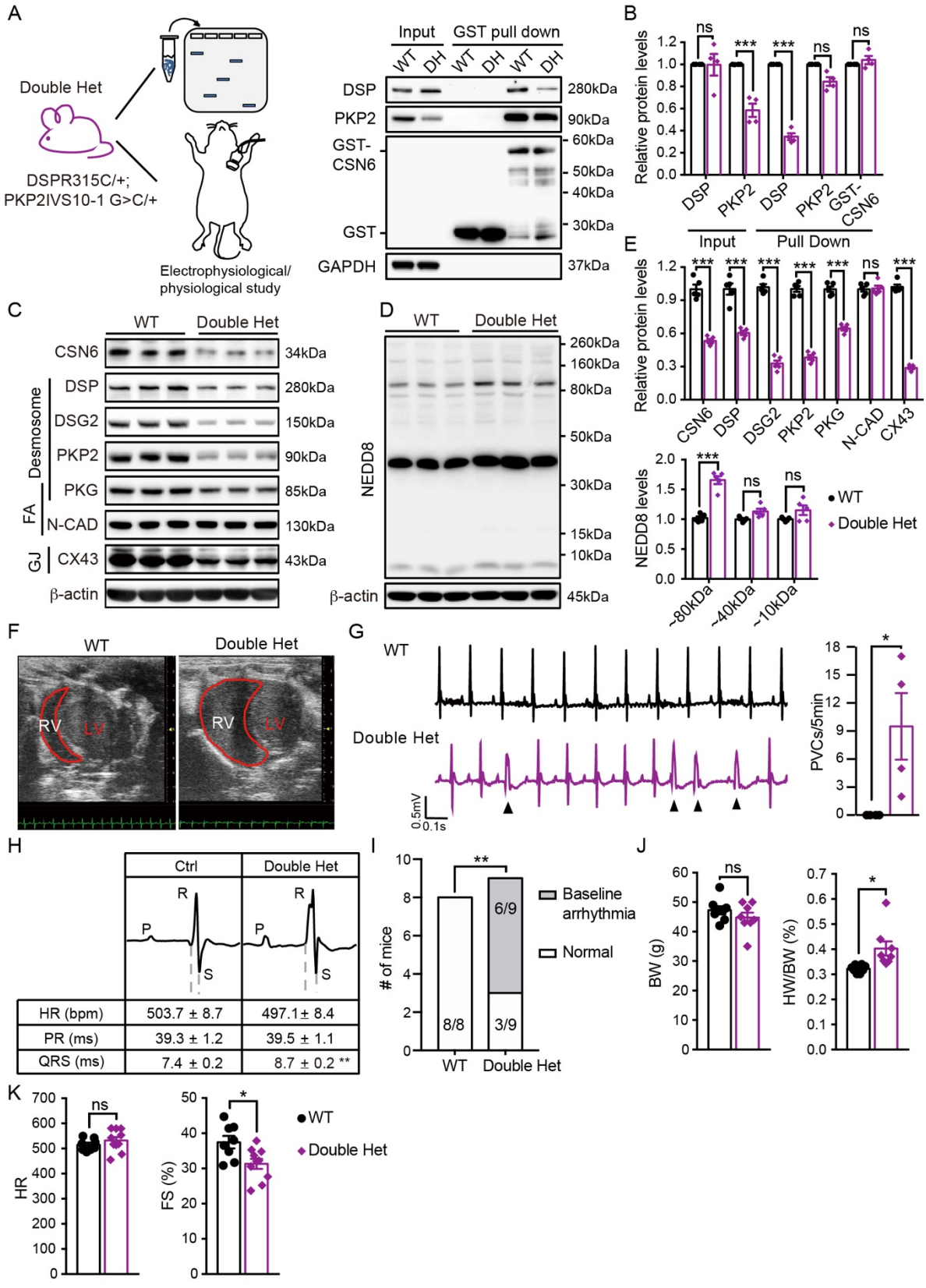
A
Double Het
DSPR315C/+;
PKP2IVS10-1 G>C/+
Electrophysiological/
physiological study
Input
GST pull down
WT
DH
DSP
PKP2
GST-CSN6
GST
GAPDH
280kDa
90kDa
60kDa
50kDa
40kDa
30kDa
37kDa
B
Relative protein levels
ns
***
E
Input
Pull Down
CSN6
DSP
DSG2
PKP2
PKG
N-CAD
CX43
NEDD8 levels
~80kDa
~40kDa
~10kDa
WT
Double Het
C
Desmosome
FA
GJ
34kDa
150kDa
85kDa
130kDa
43kDa
D
NEDD8
260kDa
160kDa
80kDa
50kDa
15kDa
10kDa
45kDa
F
RV
LV
G
PVCs/5min
0.5mV
0.1s
H
Ctrl
Double Het
R
P
S
HR (bpm)
503.7 ± 8.7
497.1± 8.4
PR (ms)
39.3 ± 1.2
39.5 ± 1.1
QRS (ms)
7.4 ± 0.2
8.7 ± 0.2 **
I
# of mice
6/9
8/8
3/9
Baseline arrhythmia
Normal
J
BW (g)
HW/BW (%)
K
HR
FS (%)

SUPPLEMENTAL DATA

Desmosomal COP9 regulates proteome degradation in arrhythmogenic right ventricular dysplasia/cardiomyopathy

Yan Liang[1], Robert C. Lyon[1], Jason Pellman[1], William H. Bradford[1], Stephan Lange[1,2], Julius Bogomolovas[1], Nancy D. Dalton[1], Yusu Gu[1], Marcus Bobar[1], Mong-Hong Lee[3], Tomoo Iwakuma[4], Vishal Nigam[5,6], Angeliki Asimaki[7], Melvin Scheinman[8], Kirk L. Peterson[1] and Farah Sheikh[1*]

[1]Department of Medicine, University of California San Diego, 9500 Gilman Drive, La Jolla, CA, 92093, USA; [2]Institute of Medicine, Department of Molecular and Clinical Medicine and Wallenberg Centre for Molecular and Translational Medicine, University of Gothenburg, Gothenburg, Sweden; [3]Department of Molecular and Cellular Oncology, The University of Texas MD Anderson Cancer Center, Houston, TX, 77030, USA; [4]Department of Cancer Biology, University of Kansas Medical Center, Kansas City, KS, 66010, USA; [5]Department of Pediatrics, University of California San Diego, 9500 Gilman Drive, La Jolla, CA, 92093, USA; [6]Department of Pediatrics, Seattle Children's Research Institute and University of Washington, 1900 Ninth Ave, Seattle, WA, 98101, USA; [7]Cardiology Clinical Academic Group, St. George's University of London, Cranmer Terrace, London, UK; [8]Department of Medicine, Cardiac Electrophysiology Section, University of California San Francisco, 500 Parnassus Avenue, San Francisco, CA, 94143, USA

Corresponding author: Farah Sheikh, Department of Medicine, University of California San Diego, 9500 Gilman Drive, La Jolla, CA, 92093-0613C. Tel: (858) 246-0754, Fax: (858) 822-1355; email address: fasheikh@health.ucsd.edu

Supplemental Figure 1

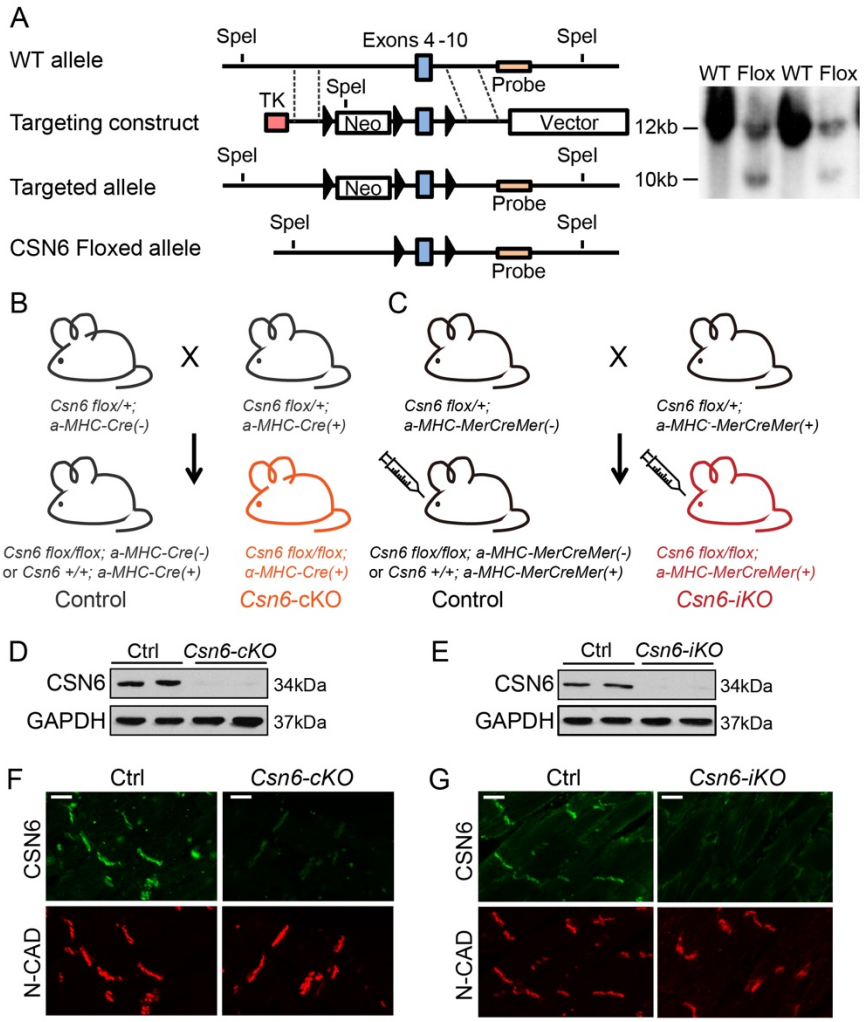

Supplemental Figure 1: Generation and validation of CSN6 loss in cardiac specific and cardiac inducible *Csn6* knockout mice. (**A**) Restriction map of the relevant genomic region of *Csn6*, targeting construct, the mutated locus following recombination and *Csn6* floxed allele (left). TK: thymidine kinase gene, Neo: neomycin resistance gene. Detection WT and mutant (target) alleles by southern blot analysis (right). (**B**) Schematic representation of breeding strategy to generate *Csn6*-cKO (*Csn6 flox/flox*; *a-MHC-Cre(+)*) and littermate control (*Csn6 flox/flox; a-MHC-Cre(-)* or *Csn6*$^{+/+}$*; a-MHC-Cre(+)*) mice. (**C**) Schematic representation of breeding strategy to generate *Csn6*-iKO (*Csn6 flox/flox; a-MHC-MerCreMer(+)*) and littermate control (*Csn6 flox/flox; a-MHC-MerCreMer(-)* or *Csn6 +/+; a-MHC-MerCreMer(+)*) mice. To induce ablation of *Csn6*, 5- to 6-week-old mice were treated with daily intraperitoneal injection of tamoxifen (Sigma, 50μg/g per day) for 5 consecutive days. (**D** and **E**) Protein blot analysis of CSN6 in total

protein extracts from *Csn6*-cKO and control mice at 2 weeks of age (**D**) and *Csn6*-iKO mice at 2 weeks post tamoxifen injection (**E**) (n=4 mice). GAPDH is used as a loading control. (**F** and **G**) Immunofluorescence staining of CSN6 (green) and N-cadherin (red) in cardiac sections from *Csn6*-cKO and control mice at 2 weeks of age (**F**) and *Csn6*-iKO at 2 weeks post tamoxifen injection (**G**). Scale Bar: 10 μm.

Supplemental Figure 2

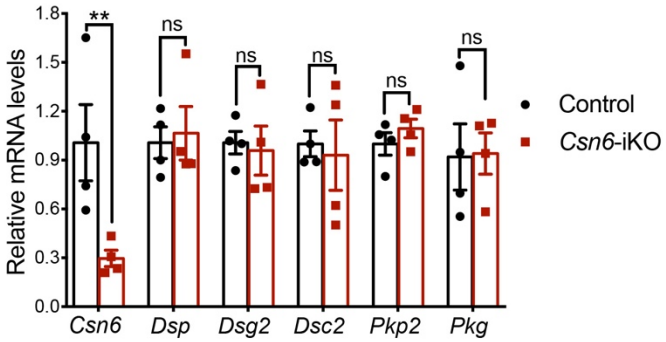

Supplemental Figure 2: RNA levels of desmosomal genes are not impacted in *Csn6* knockout hearts. Quantitative RT-PCR analysis of *Csn6* and desmosomal gene expression in *Csn*6-iKO and control mouse hearts at 6 weeks post-tamoxifen injection (n=4 mice). *18S* and *Gapdh* RNA were used as loading controls and showed similar results. Data are mean ± s.e.m; two-way ANOVA with Sidak multiple comparison test, $^{**}P<0.01$, ns, not significant.

Supplemental Figure 3

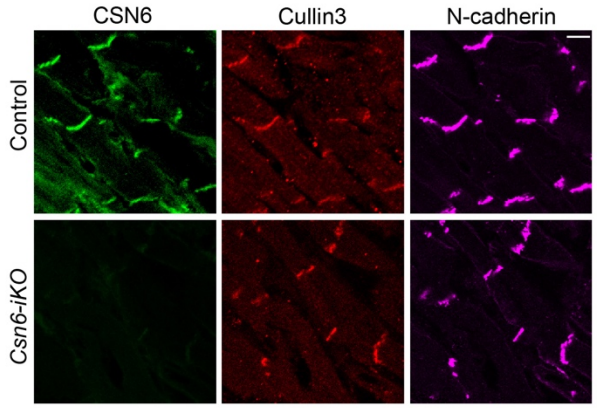

Supplemental Figure 3: Cullin 3 is localized to the cardiac cell-cell junction in adult WT and *Csn6*-iKO mouse hearts. Immunofluorescence staining of Cullin 3 (red), CSN6 (green) and N-cadherin (magenta) in control and *Csn6*-iKO mouse hearts at 6 weeks post tamoxifen injection (n=3 per group). Scale bar: 10μm.

Supplemental Figure 4

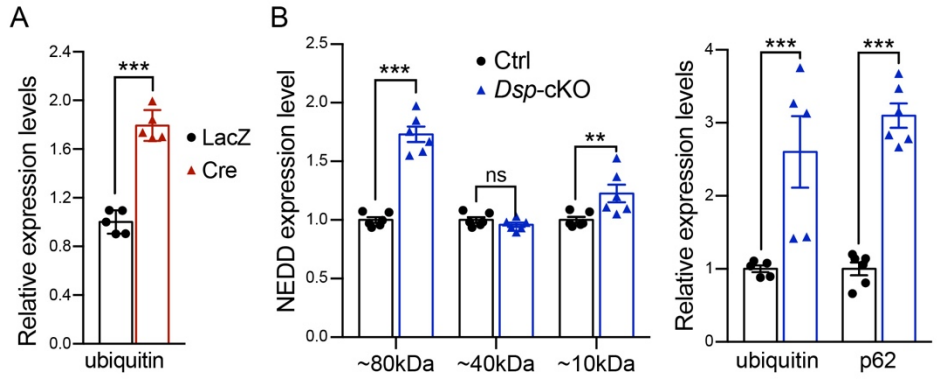

Supplemental Figure 4: Quantification of protein expression levels in Figure 4 and Figure 5. (**A**) Quantification of protein expression levels in Figure **4A**. The expression levels of the proteins were normalized to the loading control GAPDH. Data are mean ± s.e.m; two-tailed Student's t-test. ***P<0.001. (**B**) Quantification of protein expression levels in Figure **5A**. The expression levels of the proteins were normalized to the loading control GAPDH. Data are mean ± s.e.m;, two-way ANOVA with Sidak multiple comparison test, **P<0.01, ***P<0.001, ns, not significant.

Supplemental Figure 5

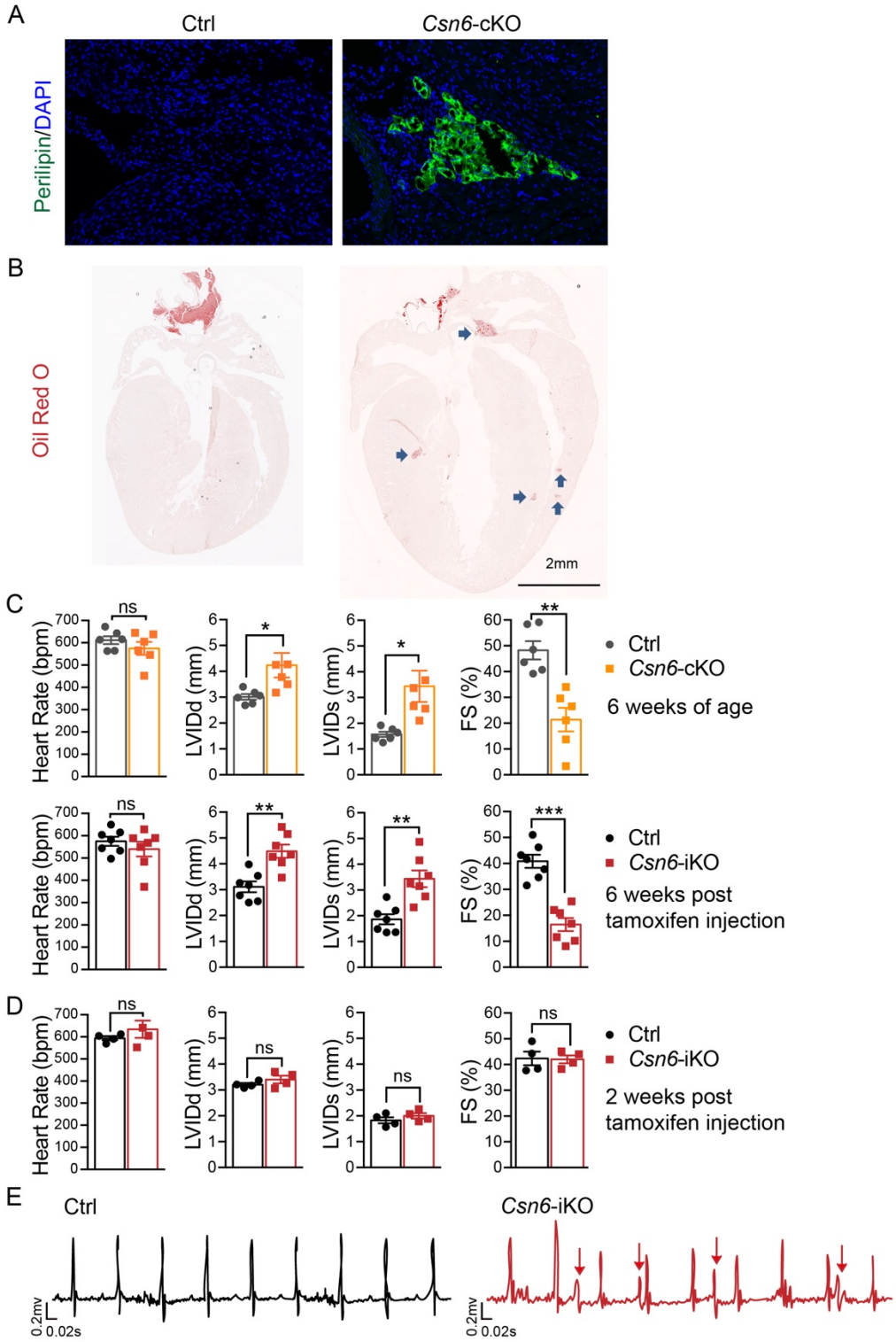

Supplemental Figure 5: Characterization of cardiac specific *Csn6* knockout mice. (**A**) Immunofluorescence staining of perilipin in triangular area of cardiac sections in *Csn6*-cKO and control mice at 6 weeks of age. Cardiac sections were counterstained with DAPI nuclear stain

(blue). Scale Bar: 100 μm. (**B**) Representative Oil Red O stained whole cardiac sections from *Csn6*-cKO and control mice at 6 weeks of age (n=4 per group). Scale bar: 2mm.(**C**) Echocardiographic M-mode analysis of heart function in *Csn6* deficient and control mice at 6 weeks of age and post-tamoxifen injection (n=6 mice). FS %: percent fractional shortening, LVIDd: left ventricular internal dimension at end-diastole. LVIDs: left ventricular internal dimension at end-systole. Data are mean ± s.e.m.; two-tailed Student's t-test, $^{*}P<0.05$; $^{**}P<0.01$; $^{***}P<0.001$; ns, not significant. (**D**) Echocardiographic M-mode analysis of heart function in *Csn6*-iKO and control mice at 2 weeks post tamoxifen injection (n=4 mice). Data are mean ± s.e.m.; two-tailed Student's t-test, ns, not significant. (**E**) Representative conscious ECG tracings from *Csn6*-iKO (red) and control mice (black) at 2 weeks post tamoxifen injection (n=4 mice). Arrows denotes ectopic beats.

Supplemental Figure 6

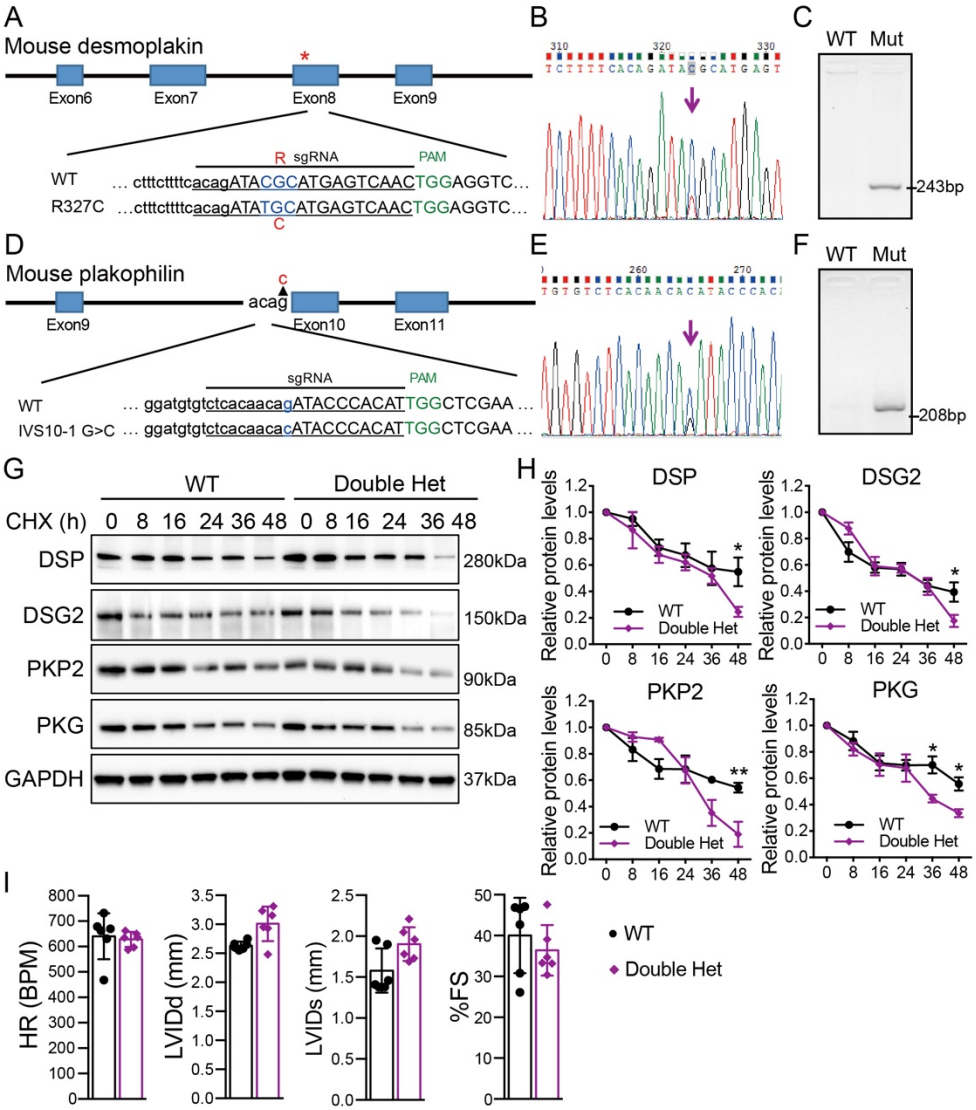

Supplemental Figure 6: Generation and characterization of knock-in mice harboring human equivalent *DSP R315C* and *PKP2 IVS10-1 G>C* mutations. (**A** and **D**) Schematic of the Cas9/sgRNA targeting site for the *Dsp R327C* (**A**) and *Pkp2 IVS10-1 G>C* (**D**) which are equivalent to the human *R315C* mutation and *PKP2 IVS10-1 G>C* respectively. The sgRNA coding sequence is underlined. The protospacer-adjacent motif (PAM) sequence is labeled in green. Uppercase: exon sequences. Lowercase: intron sequences. (**B** and **E**) Validation of *Dsp R327C* (**B**) and *Pkp2 IVS10-1 G>C* (**E**) allele by sequencing. (**C** and **F)** PCR using mutant-specific primers confirmed newborn mice contained the correct gene variant allele. (**G** and **H**) Representative protein blots (**G**) and quantification analyses (**H**) of desmosomal proteins in ventricular cardiomyocytes which isolated from Double Het and WT pups. The cardiomyocytes

were treated with cycloheximide (CHX, 10 μg/ml) for 0, 8, 16, 24, 36 and 48 hours. The expression levels of proteins were normalized to the loading control GAPDH. Data are mean ± s.e.m; two-way ANOVA with Sidak multiple comparison test, $^{*}P<0.05$, $^{**}P<0.01$. (**I**) Echocardiographic M-mode analysis of left ventricular dimensions and function in Double Het and WT mice at 4 months of age (n=6 mice). FS %: percent fractional shortening, LVIDd: left ventricular internal dimension at end-diastole. LVIDs: left ventricular internal dimension at end-systole. Data are mean ± s.e.m.; two-tailed Student's t-test.

Supplemental Figure 7

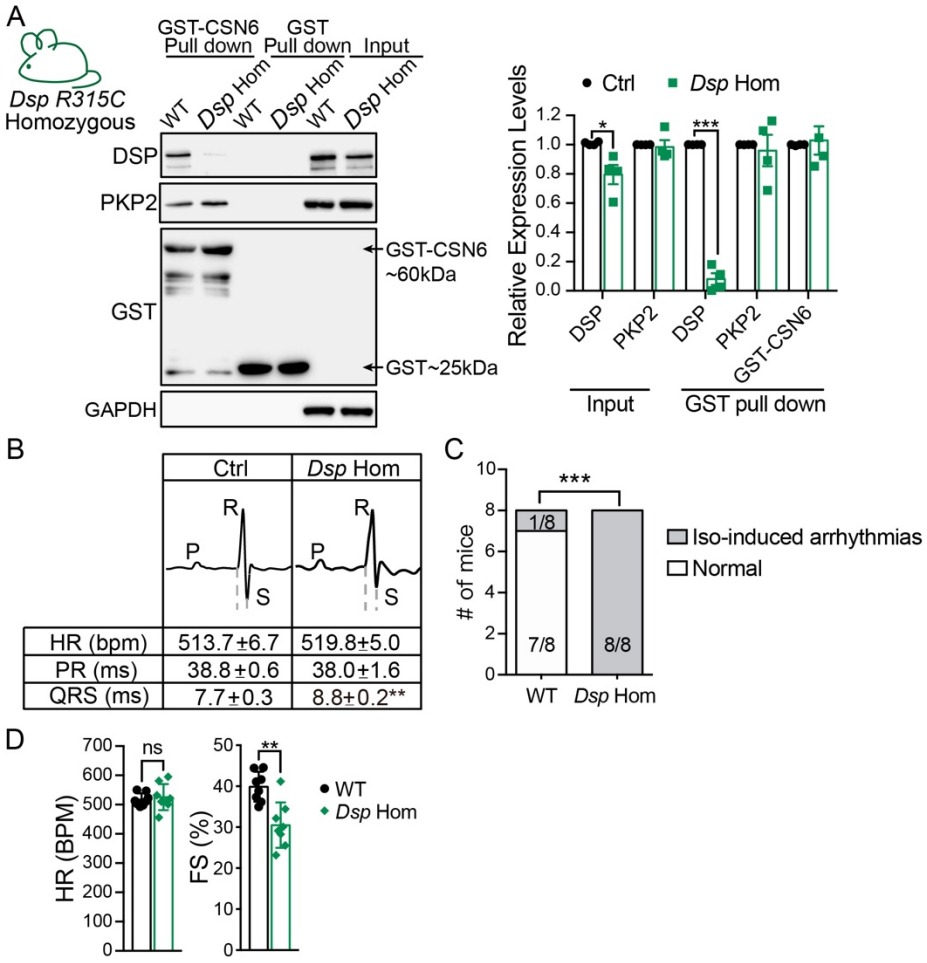

Supplemental Figure 7: Characterization of *Dsp R315C* homozygous mice. (**A**) Protein blot analyses and quantification of protein expression levels following GST pulldown assay. GST (~25kDa) and GST-CSN6 (~60kDa) protein were incubated with the heart extracts from WT and *Dsp R315C* homozygous mice (*Dsp* Hom) at 1 year of age (n=4 per group). The expression levels of input proteins were normalized to the loading control GAPDH. Data are mean ± s.e.m; two-way ANOVA with Sidak multiple comparison test, **P*<0.05, ****P*<0.001. (**B**) Representative surface ECG tracings in *Dsp R315C* homozygous and WT mice at 1 year of age (n=8 per group). Quantification of heart rate (HR), PR and QRS intervals from ECG tracings was performed. Data from 100 ECG tracings per mouse were averaged for analysis. Data are mean ± s.e.m; Student's two-tailed t-test, ***P*<0.01. QRS duration is indicated by the dotted line. (**C**) Quantification of number of *Dsp R315C* homozygous and WT mice which displayed arrhythmia with 2.5mg/kg

isoproterenol treatment during ECG recording at 1 year of age (n=8 per group). Chi-square test, ***P<0.05. (**D**) Echocardiographic M-mode analysis of left ventricular dimensions and function in *Dsp R315C* homozygous and WT mice at 1 year of age (n=8 per group). HR: heart rate; FS %: percent fractional shortening. Data are mean ± s.e.m.; Student's two-tailed t-test. **P<0.01, no significant differences.

Supplemental Table 1: *Dsp R315C* and *Pkp2 IVS10-1 G>C* crRNA, trans-activating crRNA (tracrRNA), and single-strand oligodeoxynucleotides sequences used to generate knockin mice.

Oligo Name	Sequence (5' to 3')
Dsp R315C crRNA	acagauacgcaugagucaacGUUUUAGAGCUAUGCUGUUUUG
Pkp2 IVS10-1 G>C crRNA	cucacaacagauacccacauGUUUUAGAGCUAUGCUGUUUUG
tracrRNA	AAACAGCAUAGCAAGUUAAAAUAAGGCUAGUCCGUUAUCAAC UUGAAAAAGUGGCACCGAGUCGGUGCU
Dsp R315C DNA	AACAGAAATCTAACTGTGACTTGCTGTATGGACTGGTCCTTTCTTTTC ACAGATA**T**GCATGAGTCAACTGGAGGTCAAGGAAAAGGAACTCAAT AAGCTTAAACAAGAAAG
Pkp2 IVS10-1 DNA	AGAGAACTTCTCTGGTAGCAAATGTGATAGCATTTACAGGATGTGTC TCACAACA**C**ATACCCACATTGGTGGCTCGAATGGTTGTCCAAAAGGA AAATGGTCTTCAGCATA

Supplemental Table 2: Primer sequences for real-time PCR analyses.

Gene	Primer 5'-3'
Csn6-F	GAGCTGGAGTTTCTGGGTTG
Csn6-R	GATCCGTTCAGCTTCCTCAG
Dsp-F	GCTCCATTACCAAGACTTCATC
Dsp-R	TGTCGTCGTCTCCAAACATCT
Dsg2-F	GAGGAATTGAGTGCAGCACATAC
Dsg2-R	CTTGCTTCCACCGTCAAGG
Dsc2-F	ATGCAGATGGGAGAAGCTGT
Dsc2-R	TGCAACAATTTCAGCAGAGG
Pkp2-F	GGCTCTCCAGAACCTCACAG
Pkp2-R	GGGAAAGATTCCGTGACAAA
Pkg-F1	CCTGTGGACTCTGCGCAAT
Pkg-R1	GACCAGGATCTTCAGCACACTCT

Figure 8: Human desmosomal mutations that destabilize CSN6 are sufficient to disrupt CSN6 expression, neddylation and trigger ARVD/C features in mice. (**A** and **B**) Protein blot analyses (**A**) and quantification of protein expression levels (**B**) following GST pulldown assay. GST (~25kDa) and GST-CSN6 (~60kDa) protein were incubated with the heart extracts from WT and Double Het mice at 4 months of age (n=4 per group). The expression levels of input proteins were normalized to the loading control GAPDH. Data are mean ± s.e.m; two-way ANOVA with Sidak multiple comparison test, ***P<0.001, ns, not significant. (**C-E**) Protein blot analysis of cardiac cell-cell junction proteins (**C**), NEDD8 expression levels (**D**) and quantification of protein expression levels (**E**) in right ventricular insoluble extracts from Double Het and WT mice at 4 months of age (n=5 per group). The expression levels of proteins were normalized to the loading control β-actin. Data are mean ± s.e.m; two-way ANOVA with Sidak multiple comparison test, ***P<0.001, ns, not significant. (**F**) Representative apical four chamber views from echocardiography ((n=6 per group) at 4 months of age. (**G**) Representative surface ECG tracing and quantification of premature ventricular contractions (PVCs) (n=4 per group) at 4 months of age. Data are mean ± s.e.m; Student's two-tailed t-test. Arrows denote PVCs. *P<0.05. (**H**) Representative surface ECG tracings in Double Het and WT mice at 1 year of age (n=8-9 per group). Quantification of heart rate (HR), PR and QRS intervals from ECG tracings was performed. Data from 100 ECG tracings per mouse were averaged for analysis. Data are mean ± s.e.m; Student's two-tailed t-test, **P<0.01. QRS duration is indicated by the dotted line. (**I**) Quantification of number of Double Het and WT mice which displayed baseline arrhythmia during ECG recording at 1 year of age (n=8-9 per group). Chi-square test, *P<0.05. (**J**) Body weight (BW) and heart weight to body weight ratios (HW/BW) from Double Het and WT mice at 1 year of age (n=8 per group). Data are mean ± s.e.m; Student's two-tailed t-test. *P<0.05, ns, not significant. (**K**) Echocardiographic M-mode analysis of left ventricular dimensions and function in Double Het and WT mice at 1 year of age (n=8-10 per group). HR: heart rate; FS %: percent fractional shortening. Data are mean ± s.e.m.; Student's two-tailed t-test. *P<0.05, no significant differences.